

www.acsami.org Research Article

# Atomic Layer Deposited Ni/ZrO<sub>2</sub>-SiO<sub>2</sub> for Combined Capture and Oxidation of VOCs

Busuyi O. Adebayo, Kyle Newport, Han Yu, Ali A. Rownaghi, Xinhua Liang, and Fateme Rezaei\*



Cite This: ACS Appl. Mater. Interfaces 2020, 12, 39318–39334



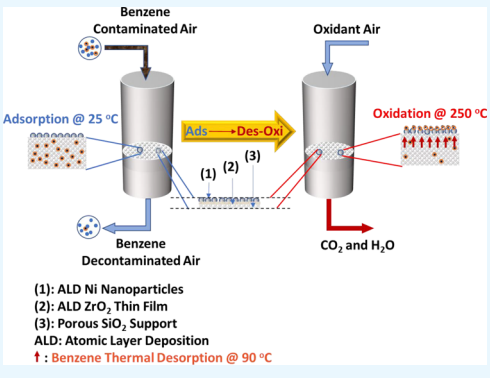
**ACCESS** 

Metrics & More

Article Recommendations

Supporting Information

ABSTRACT: This work reports on the development of novel Ni nanoparticle-deposited mixed-metal oxides  $ZrO_2$ –SiO<sub>2</sub> through atomic layer deposition (ALD) method and their application in combined capture and oxidation of benzene, as a model compound of aromatic VOCs. Concentrating ppm-level VOCs in situ, before their oxidation, offers a practical approach to reduce the catalyst inventory and capital cost associated with VOC emissions abatement. The benzene vapor adsorption isotherms were measured at 25 °C and in the pressure range of 0 to benzene saturation vapor pressure thereof (0.13 bar). In the combined capture-reaction tests, the materials were first exposed to ca. 86 100 ppm, benzene vapor at 25 °C, followed by desorption and catalytic oxidation while raising the bed temperature to 250 °C. The textural properties revealed that ALD of Ni or  $ZrO_2$  on  $SiO_2$  decreased surface area and pore volume, while sequential doping with  $ZrO_2$  and then Ni caused the otherwise. The benzene vapor adsorption isotherms



followed the type-IV isotherm classification, revealing a combination of monolayer-multilayer and capillary condensation adsorption mechanisms in sequence. At saturation vapor pressure, an average equilibrium adsorption capacity of 15 mmol/g was obtained across the materials. However, the dynamic adsorption capacities were up to 50% less than the corresponding equilibrium uptake for the materials. Benzene desorption temperature was observed around 90 °C, and conversion of 85–95% and TOF of 1.28–16.42 mmol $_{C6H6}/mol_{Ni}/s$  were obtained over the materials, with  $3Ni/ZrO_2-SiO_2$ , prepared with 3 ALD cycles, exhibiting the maximum conversion and TOF indicating synergistic effects of Ni nanoparticles and  $ZrO_2$  support based on the number of ALD cycles. However, the yields of  $CO_2$  and  $H_2O$  were about 5% and 40%, respectively. The small value of the  $CO_2$  yield was hypothesized to be due to simultaneous high-temperature adsorption of  $CO_2$  as the catalytic reaction progressed. The high adsorption affinity, low desorption temperature, and high catalytic activity of the materials investigated in this study made these materials as promising candidates for the abatement of BTX.

KEYWORDS: VOC, adsorption, oxidation, mixed-metal oxide, ALD

# 1. INTRODUCTION

Aromatic hydrocarbons such as benzene, toluene, and xylene (BTX) are human carcinogens and one of the largest emissions among volatile organic compounds (VOCs).1 Traditionally, these compounds are removed from air or process streams by thermal and catalytic combustion, or adsorption, although other methods such as biofiltration and absorption have also been attempted as well.<sup>2,3</sup> Despite significant advances in the VOCs abatement technologies, they still suffer from significant shortcomings. For instance, although adsorption is proven to be efficient for the removal of VOCs from low to ultralow concentrated streams, its efficiency deteriorates under humid conditions. Moreover, while thermal oxidation suffers from high energy demand, catalytic oxidation suffers from high catalyst inventory coupled with catalyst deactivation (fouling/ coking, poisoning, and aging/sintering). Therefore, there is still a need for further improvement in such technologies.

To address the drawbacks of the current technologies, integrated abatement processes such as adsorptive reactors are

being investigated. Process intensification through adsorptive reactors offers the opportunity to reduce capital investment, catalyst inventory, and requirements for external energy supply or cooling capacity. In the combined adsorption-catalysis approach, adsorbate is first concentrated via adsorption, after which combustion takes place whereby the adsorbed VOCs are converted in situ to H<sub>2</sub>O and CO<sub>2</sub>. For instance, Kullavanijaya et al.<sup>4</sup> used this integrated strategy to concentrate a VOC-laden stream over a solid adsorbent in the adsorption bed at low temperature before it was combusted directly or catalytically in an incinerator for conversion to harmless compounds. In their later work, Kullavanijaya et al.<sup>5</sup> treated binary VOC mixtures

Received: June 27, 2020 Accepted: August 10, 2020 Published: August 10, 2020





first by adsorption on an activated carbon followed by catalytic reactions on a palladium-coated CeO<sub>2</sub>/Al<sub>2</sub>O<sub>3</sub>. Similarly, Nikolajsen et al.<sup>6</sup> investigated the performance of sequential adsorption and oxidation of a dilute VOC-laden air stream using a sintered-metal-fiber (SMF) supported adsorbent-catalyst. Recently, Wang et al.<sup>7</sup> successfully used a combined adsorption-combustion method to eliminate bulky aromatics (toluene, o-xylene, and 1,3,5-trimethylbenzene) over bifunctional Ru/HZSM-5. Moreover, the applicability, feasibility, and potential advantage of an adsorptive reactor for VOCs abatement had also been studied via numerical modeling.<sup>8</sup> One of the most crucial aspects of the combined approach is the proper selection of materials for improved performance.

To date, different materials have been evaluated for adsorption and/or catalytic oxidation of VOCs from industrial wastes and polluted air including carbon-based materials, zeolites, metal—organic frameworks (MOFs), and metal oxides. The best materials for catalytic oxidation of VOCs are noble metals (prominently Pd, Pt, Ru, Rh, Ir, Os, Ag, and Au) in terms of activity, selectivity, and stability. However, noble metals are very expensive and prone to poisoning, leading to research for more cost-effective alternatives such as transition metal oxides (e.g., Ti, Zr, Al, Ni, Cu, Fe, and Zn). Unfortunately, single transition metal oxides are less active and stable compared with noble metals. Incorporating another transition metal into an existing metal oxide forms mixed-metal oxides (MMOs) in which the synergistic effects enhance their catalytic activities significantly.

Nickel-based catalysts such as Ni/Al<sub>2</sub>O<sub>3</sub>, Ni/CeO<sub>2</sub>, and Ni/ SiO<sub>2</sub> have been widely studied for the oxidation of VOCs mainly because they are cheap and abundant, resistant to poisoning, and environmentally benign and exhibit comparable catalytic performance to that of noble metals. For instance, Tang et al. 16 demonstrated the use of NiO nanoparticles for total oxidation of benzene and reported the conversion of ~98% at 350 °C. Similarly, Bai et al. 17 used porous NiO nanoflowers and nanourchins as a catalyst for complete oxidation of toluene. Their results indicated a toluene conversion of about 100% at a temperature as low as 250 °C. Generally, the catalytic performance of Ni-based catalysts depends on the nature of the support among other factors. Furthermore, various attempts are still being made to further improve the catalytic performance of these materials by surface modification.

Atomic layer deposition (ALD) is a promising technique to prepare MMOs, and it is very suitable and efficient for this application since it is a surface controlled layer-by-layer coating process based on self-limiting surface reactions, and it has been utilized to deposit metal oxide films with nanometer-sized control.20 For instance, Lee et al.21 demonstrated that ALDcoated TiO2 thin films on a nanostructured Al2O3 membrane anode showed high toluene adsorption capacity and selectivity. They recorded dynamic adsorption capacity as high as 277 mg/g. In a similar work by Eun et al., 20 toluene oxidation was catalyzed by ALD-prepared NiO/SiO<sub>2</sub> and NiO/TiO<sub>2</sub>/SiO<sub>2</sub> under dry and 70% relatively humid conditions at 250 and 350 °C. While NiO/TiO<sub>2</sub>/SiO<sub>2</sub> showed excellent performance at all conditions, NiO/SiO<sub>2</sub> showed a reduced performance at 250 °C under humid condition. In a study conducted by Liotta et al., 13 supported noble metals were used for hybrid adsorption catalysis of VOCs. They reported higher performance due to the synergetic effects of the doped heteroatoms. Despite the scientific proof of the potential of thin-film

materials as adsorbent and/or catalyst for abatement of VOCs,  $^{22}$  the use thereof is still scarcely reported in the literature.

In this study, we explored the concerted advantages offered by hybrid adsorption-catalysis and ALD methods. Previously in our lab, porous titania and zirconia silica materials were prepared by the one-pot (cosynthesis) sol-gel method.<sup>23</sup> The materials depicted good surface characteristics with excellent benzene adsorption performance. Aiming at developing novel dual-functional materials with excellent adsorptive and catalytic performances, we embarked on a study to incorporate nickel on zirconia silica (Ni/ZrO<sub>2</sub>-SiO<sub>2</sub>), and, for comparison, on bare porous silica (Ni/SiO<sub>2</sub>). These materials were synthesized by Ni ALD on SiO<sub>2</sub> and ZrO<sub>2</sub>-SiO<sub>2</sub> supports with varied Ni loadings, and ZrO2-SiO2 supports were prepared by depositing an ultrathin ZrO2 film on porous SiO2 particles by ALD. The materials were then tested for their adsorption capacities and thereafter evaluated for the sequential hybrid adsorption and catalytic oxidation of benzene as the candidate BTX compound. To the best of our knowledge, this work provides the first detailed evaluation of ALD coated samples in combined capture-oxidation of aromatic VOCs.

#### 2. EXPERIMENTAL SECTION

**2.1. Materials.** Ammonium hydroxide (NH $_3$ OH, 28.4%) was purchased from Fisher-Scientific. All other chemicals used in this work including titanium(IV) butoxide (97%, TiB), tetraethyl orthosilicate (99%, TEOS), polyethylene glycols (PEG), zirconium-(IV) propoxide (70% ZrP in 1-propanol), triethanolamine (98%, TEAH), hexadecyltrimethylammonium bromide (CTAB), nitric acid (70% HNO $_3$ ), tetrakis(dimethylamido)zirconium(IV) (Zr(NMe $_2$ ) $_4$ , electronic grade,  $\geq$  99.99%), and bis(cyclopentadienyl)nickel(II) (Ni(cp) $_2$ ) were purchased from Sigma-Aldrich. Ultrahigh purity oxygen, hydrogen, nitrogen, and helium gases were purchased from Airgas. All chemicals and gases were used as purchased without further purification.

**2.2. Materials Synthesis.** First, porous UVM-7-like silica support was synthesized by following a detailed procedure reported in our previous work.<sup>23</sup> An ultrathin ZrO<sub>2</sub> film and highflyer dispersed Ni nanoparticles were deposited on the porous silica supports via ALD using a homemade fluidized bed reactor, the details of which are described elsewhere.<sup>24</sup> Before the ALD process, the synthesized silica was outgassed at 200  $^{\circ}\text{C}$  for 3 h under vacuum. Thereafter, Ni/SiO $_2$ was prepared by depositing Ni nanoparticles on the outgassed silica using ALD. A typical Ni ALD cycle consisted of a Ni(cp)2 dose, followed by an N2 flush, which was followed by an H2 dose, and, finally, an N<sub>2</sub> flush. A temperature of 300 °C was maintained for Ni ALD reaction. Ni(cp)2 was delivered into the reactor after it was heated to 100 °C. For the Ni/ZrO2-SiO2 materials, ZrO2 film was first deposited on SiO2 through 5 cycles of ALD and subsequently Ni ALD on the outgassed porous silica. A typical ZrO2 ALD coating cycle consisted of a Zr(NMe<sub>2</sub>)<sub>4</sub> dose, followed by an N<sub>2</sub> flush, which was followed by a deionized water dose and, finally, an N2 flush. A temperature of 250 °C was maintained for ZrO<sub>2</sub> ALD, and  $Zr(NMe_2)_4$  was delivered into the reactor after heating to 80 °C. The samples were named as bare SiO<sub>2</sub> and ZrO<sub>2</sub>-SiO<sub>2</sub> (group-0 materials), xNi/SiO<sub>2</sub> (group-1 materials), and xNi/ZrO<sub>2</sub>-SiO<sub>2</sub> (group-2 materials) where "x" denotes the number of the number of ALD cycles used for Ni deposition on the materials.

**2.3. Materials Characterization.** High-angle  $(5-90^\circ)$  powder X-ray diffraction (XRD) was carried out on each sample on a PANanalytical X'Pert multipurpose X-ray diffractometer using Cu K $\alpha$  radiation ( $\lambda_1 = 1.5406$  Å,  $\lambda_2 = 1.5444$  Å with K $\alpha_2/\mathrm{K}\alpha_1 = 0.5$ ) with a scan rate of  $2\theta = 0.7^\circ/\mathrm{min}$  in order to determine the phase composition and crystallinity of the sample. In order to eliminate any background noise from the XRD analysis, zero diffraction silicon plates (SIL'TRONIX) were used for the XRD measurement. To

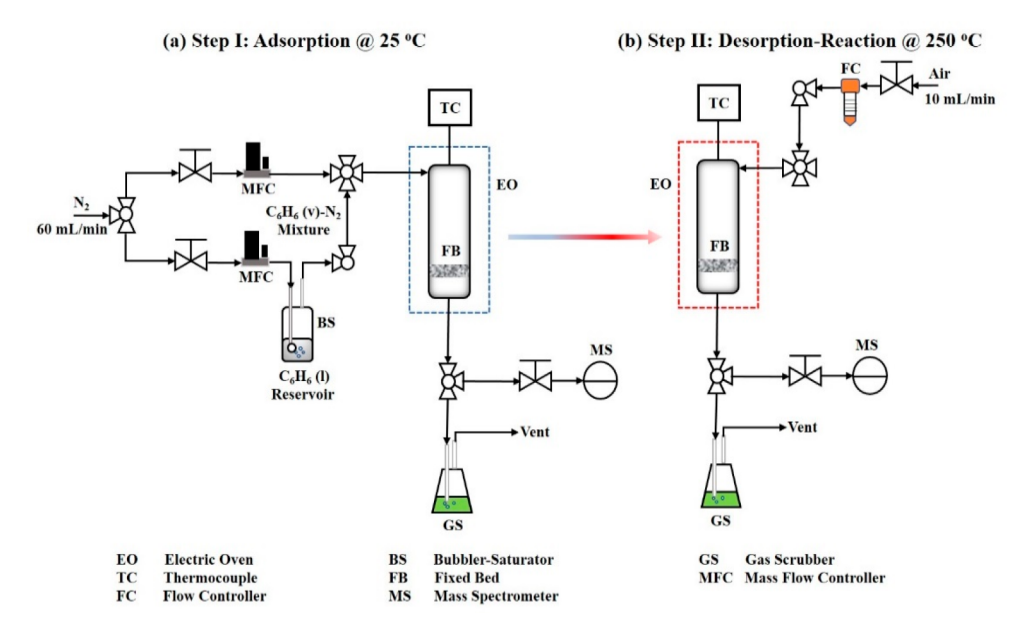


**Figure 1.** Schematic of the single-column hybrid adsorption catalytic oxidation experiment for (a) adsorption at 25 °C and (b) desorption-reaction at 250 °C.

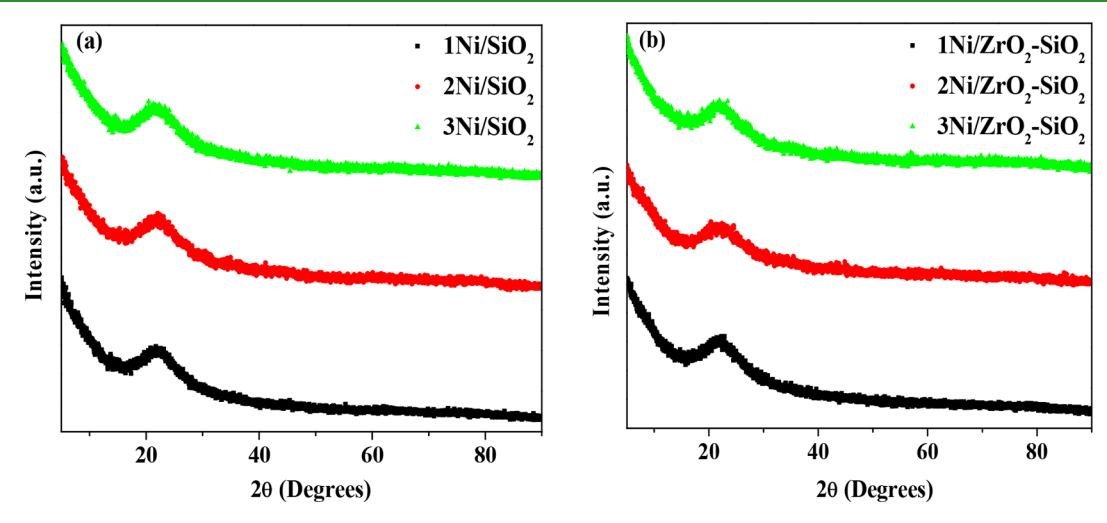


Figure 2. High-angle XRD patterns of (a) xNi/SiO<sub>2</sub> and (b) xNi/ZrO<sub>2</sub>-SiO<sub>2</sub>.

assess the textural properties of the samples, N2 physisorption (adsorption-desorption) isotherms were measured at -196 °C on a static volumetric adsorption system (Micromeritics 3Flex). Prior to the measurement, ca. 100 mg of the sample was degassed at 250  $^{\circ}\text{C}$  in Micromeritics Smart VacPrep under vacuum for 12 h. From the isotherm, the material surface area was determined by using the linearized Brunauer-Emmett-Teller (BET) model in the relative pressure range of  $0.05 < P/P_0 < 0.3$ , whereas density functional theory (DFT) cylindrical geometry classical N2-Hasley model was used to determine the pore size, pore volume, and pore size distribution (PSD). Moreover, scanning electron microscopy (SEM) was performed on each sample on a Zeiss Merlin Gemini field emission microscope (FE-SEM). Energy dispersive spectroscopy (EDS) spectra were collected on a Bruker 5030 X-Flash diffractometer using an accelerating voltage of 25 kV to qualify the surface elemental compositions and mappings of the group-1 and group-2 materials. However, to quantify the surface elemental compositions and determine the surface elemental chemical states on the group-1 and group-2 materials, X-ray photoelectron spectroscopy (XPS) spectra were collected on a Kratos Axis 165 photoelectron spectrometer with an aluminum X-ray source. Finally, to gain insight into and assess the surface acidity of the prepared samples, ammonia temperatureprogrammed desorption (NH $_3$ -TPD) was performed by first degassing the samples at 400 °C for 1 h, then cooled to 80 °C under He flow, subsequent exposure to 5% NH $_3$ /He flow at 30 mL/min for 30 min, followed by the removal of physisorbed NH $_3$  under He flow, and ramping the temperature from 80 to 800 °C at the rate of 10 °C/min.

**2.4. Benzene Vapor Adsorption Isotherm Measurements.** As one of the first steps in determining the suitability of a material for any separation/purification process, equilibrium adsorption capacity should be determined. Here, the benzene vapor adsorption isotherms were measured volumetrically at 25 °C on the 3Flex Micromeritics gas analyzer. The vapor was generated from liquid benzene at 25 °C and 1 bar and was thereafter purified to remove any trapped gas impurities and then vaporized at 25 °C using the freeze—thaw purification method described elsewhere. The liquid benzene reservoir was immersed in a water bath to keep the temperature in the sampling chamber at 25 °C for the duration of the experiment. In each measurement, about 100 mg of the sample was degassed at 250 °C under vacuum for 6 h and then cooled to 25 °C before being transferred to the Micromeritics 3Flex for the isotherm measurement.

**2.5.** Adsorption Breakthrough Experiments. The dynamic adsorption of benzene vapor on each of the samples was assessed by a

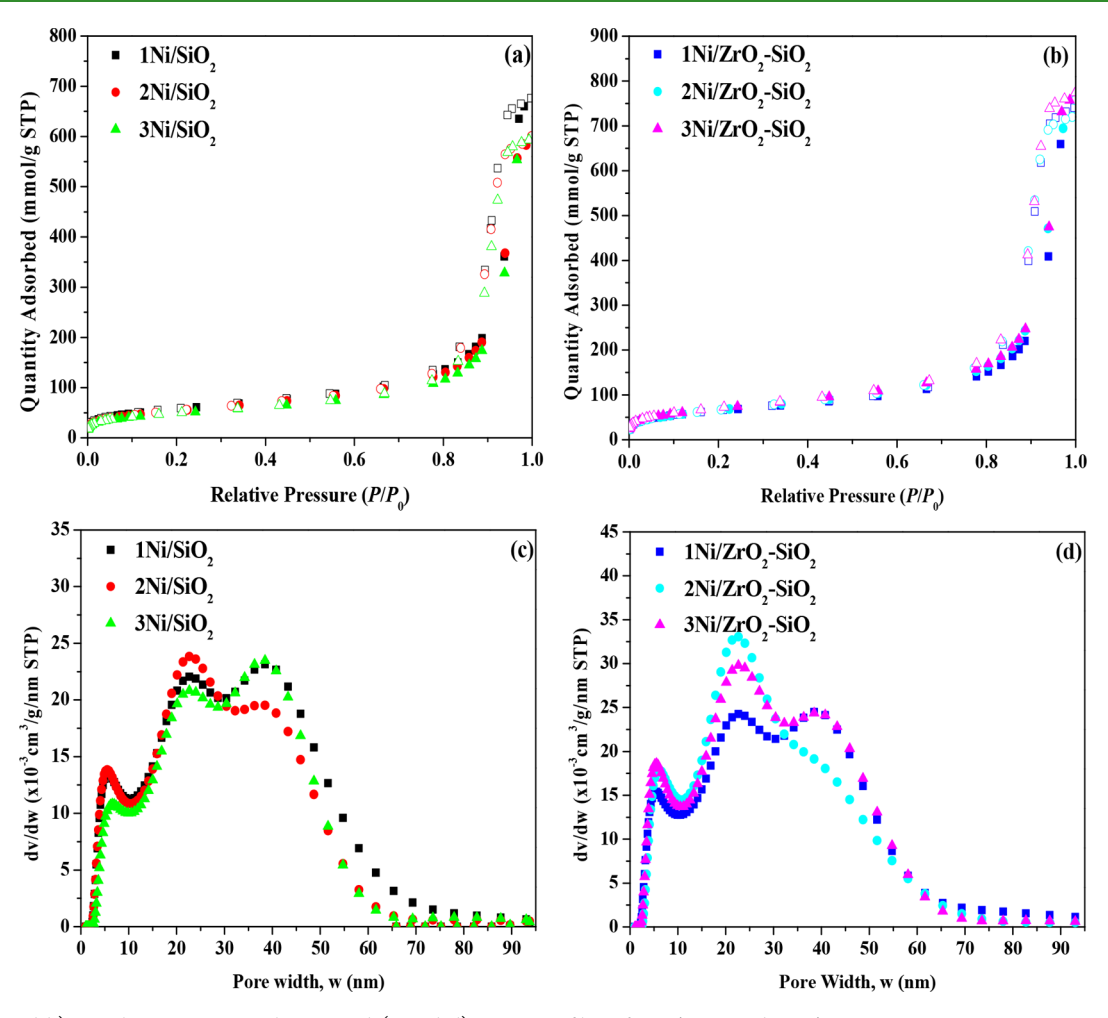


Figure 3. (a and b) N<sub>2</sub> physisorption isotherms and (c and d) PSDs profiles of xNi/SiO<sub>2</sub> and xNi/ZrO<sub>2</sub>-SiO<sub>2</sub>.

breakthrough experiment at 25 °C and 1 bar in a glass column setup depicted in panel a of Figure 1. The system flow rates were controlled by mass flow controllers (Brooks Instrument), while the adsorption temperature was controlled by a K-type thermocouple, heating tape, and an Omega benchtop controller. About 400 mg of the material under test was packed into the column and then pretreated in situ by degassing at 250 °C for 1 h under a 40 mL/min  $N_2$  flow. Thereafter, the column was cooled to the adsorption temperature followed by temperature stabilization for about 15 min. The benzene vapor was carried over to the bed by passing a  $N_2$  stream through a saturator filled with liquid benzene at a flow rate of 60 mL/min. The bed outlet concentration during adsorption was analyzed online by a mass spectrometer (MS, BELMass).

2.6. Combined Adsorption-Reaction Experiments. The desorption-reaction step was immediate and sequential to the adsorption step. At the attainment of dynamic adsorption saturation (i.e.,  $C_{\text{out}}/C_{\text{in}} = 1$ ), the process was switched from the adsorption step (Figure 1a) to the desorption-reaction step (Figure 1b). Here, regenerative air at a flow rate of 10 mL/min was fed in continuously as an inlet feed to the fixed bed, while the temperature of the system was simultaneously ramped to the required combustion temperature of 250 °C. Data acquisition of the bed outlet concentration during the catalytic reaction was continued online by the same mass spectrometer (MS, BELMass). The materials' catalytic oxidation performance was assessed based on reactant (C<sub>6</sub>H<sub>6</sub>) conversion and turnover frequency (TOF) and products (CO2 and H2O) yields and selectivities. The instantaneous and overall values of these variables were calculated based on the equations described in the Supporting Information.

# 3. RESULTS AND DISCUSSIONS

**3.1. Materials Characterization.** Shown in Figure 2 are the high-angle XRD patterns of the group-1 and group-2 materials, while that of the bare SiO2 is shown in Figure S1 in the Supporting Information. High-angle XRD was used here because it has been proven to contain a characteristic diffraction peak of silica, be it natural or synthetic around  $2\theta$ = 22-23°. Accordingly, all of the samples depicted the silica characteristic diffraction peak around angle  $2\theta = 23^{\circ}$  and has been indexed as the plane (101).<sup>27</sup> However, the peak was broad/diffuse, indicating that the materials are amorphous and therefore lack any long-range orderly arrangement of atoms. Using the Scherrer equation in conjunction with the XRD data, the average crystallite size of the synthesized materials was estimated to be about 33 nm. As can be seen in Figures 2 and S1, ZrO<sub>2</sub> coating and/or Ni nanoparticles on the silica support did not result in any noticeable change in the XRD pattern of the bare silica. This observation has been attributed to the ultrathin ZrO2 film and/or highly dispersed Ni nanoparticles on the support, implying that the ZrO<sub>2</sub> films were amorphous or that the Ni nanoparticles were well dispersed thereon.<sup>28</sup> Moreover, it is worth mentioning that the XRD patterns of the ALD coated materials did not show any significant differences among themselves relative to ZrO2 and/or Ni loading. In general, the peak observed in all of these materials is the typical broad peak observed in UVM-7 due to the secondary pore in the meso-macropore borderline.<sup>29</sup>

The N<sub>2</sub> physisorption isotherms and the pore size distributions (PSDs) of the group-1 and group-2 materials are presented in Figure 3, while those of the group-0 materials are shown in Figure S2a,b in the Supporting Information. The N<sub>2</sub> physisorption isotherms showed no difference as was similarly seen in the XRD patterns. Generally, it is evident from the isotherms that all of the materials depicted the type IV isotherm according to IUPAC classification. 30 The N2 isotherms could be described by three stages of adsorption: monolayer adsorption, multilayer adsorption, and saturation adsorption. The first and monolayer adsorption occurred in the range of  $P/P_0 \le 0.08$ , the second and multilayer adsorption in the range of  $0.08 \le P/P_0 \le 0.7$ , while the last and saturation adsorption occurred in the range  $P/P_0 > 0.7$ . The last and saturation adsorption is associated with capillary condensation of N<sub>2</sub> taking place within the pores in the mesopore range.<sup>31</sup> Moreover, all the isotherms showed type H1 hysteresis, an indication of the presence of relatively large cylindrical pores within the materials.<sup>32</sup> It is pertinent to also mention that the N<sub>2</sub> physisorbed values were relatively constant over each group of materials. From the PSD profiles, we could see that all the materials are heterogeneous with trimodal porosity having peaks centered about 5.5, 25, and 40 nm, as can be seen in Figure 3c,d. However, the PSDs remained relatively similar across all the materials. This is in agreement with the work of Smått et al.<sup>33</sup> where a similar synthesis route was used for the silica support.

Table 1 summarizes the textural properties of all the materials estimated from the  $N_2$  physisorption data. As

Table 1. Textural Properties of the Materials

sample	BET surface area $(m^2/g)$	DFT pore volume (cm <sup>3</sup> /g)	DFT pore diameter (nm)
bare SiO <sub>2</sub>	300	1.27	5.7, 23.1, 39.5
$ZrO_2$ - $SiO_2$	232	0.88	5.8, 23.1, 39.5
1Ni/SiO <sub>2</sub>	207	0.87	5.7, 23.1, 39.5
2Ni/SiO <sub>2</sub>	197	0.82	5.8, 23.1, 39.5
3Ni/SiO <sub>2</sub>	176	0.81	6.0, 23.1, 39.5
$1 \text{Ni}/\text{ZrO}_2 - \text{SiO}_2$	231	0.94	6.0, 21.5, 43.5
$2Ni/ZrO_2-SiO_2$	242	0.98	5.9, 21.5, 43.5
$3Ni/ZrO_2-SiO_2$	254	1.04	5.8, 21.5, 43.5

expected, the SiO<sub>2</sub> support has the highest surface area and pore volume, while the incorporation of cycles of ZrO2 on the SiO<sub>2</sub> support reduced those properties. Among the group-1 materials, the surface area and pore volume decreased with Ni loading, 1Ni/SiO<sub>2</sub> has 207 m<sup>2</sup>/g and 0.87 cm<sup>3</sup>/g, 2Ni/SiO<sub>2</sub> has  $197 \text{ m}^2/\text{g}$  and  $0.82 \text{ cm}^3/\text{g}$ , while  $3\text{Ni/SiO}_2$  has  $176 \text{ m}^2/\text{g}$  and 0.81 cm<sup>3</sup>/g. A similar trend was also observed in pore diameter, albeit less significantly. The progressive reduction in the surface area and pore volume observed among the group-1 materials could be explained from two different perspectives: pore-blocking leading to reduced pore size and Ni higher density with loading. However, the group-2 materials depicted a contrary trend in surface area and pore volume: 1Ni/ZrO<sub>2</sub>- $SiO_2$  has 231 m<sup>2</sup>/g and 0.94 cm<sup>3</sup>/g, increased to 242 m<sup>2</sup>/g and 0.98 cm $^3$ /g for 2Ni/ZrO $_2$ -SiO $_2$ , and finally to 254 m $^2$ /g and 1.04 cm $^3$ /g for 3Ni/ZrO $_2$ -SiO $_2$ . The improvement in surface properties observed in the group-2 materials as Ni loading increased could be ascribed to the strong Ni-ZrO2 interaction and possible changes in surface morphology, e.g., surface defects (cuts, kinks, and steps). Goma et al. doped Ni on

ZrO<sub>2</sub>/CeO<sub>2</sub> support and obtained a similar improvement in surface properties.<sup>34</sup> Comparing the group-1 and group-2 materials, the surface area and the pore volume were relatively higher in the group-2 materials than in the group-1 materials due to the Ni-ZrO<sub>2</sub> interaction effect. This was not unexpected because, as loading increased, the BET area should decrease proportionately. A similar trend had earlier been reported by Seo et al.<sup>35</sup> However, we can see that the two larger pores were relatively intact across all the materials, while the smaller pore experience little-to-no changes with loadings. Moreover, it should be mentioned that there were no significant differences in the pore sizes and pore size distributions of these materials probably because of the limited number of cycles of ALD administered on the bare silica.

The morphology of the group-1 and group-2 materials observed via SEM is shown in Figure 4. Higher magnification (ca. 1 order of magnitude higher) was used for the group-2 materials compared to the group-1 materials in order to resolve the ZrO<sub>2</sub> film. The first thing that is immediately noticeable in these images is the marked porosity of the materials. Figure 4a-c revealed that the pores are interconnected and spongelike, being characteristic of UVM-7,31 with an estimated pore size of ca. 20 nm, which closely corresponds with the larger pore diameter set shown in Table 1, while Figure 4d-f revealed that the pores are somewhat cylindrical as first revealed by the type H1 adsorption—desorption hysteresis loop observed via the N<sub>2</sub> physisorption in Figure 3a,b. Moreover, Figure 4d-f clearly confirmed a homogeneous, crack-free, and nonporous ZrO<sub>2</sub> ALD-coated film around a porous block of particles in all the group-2 materials. The film thickness was estimated to be about 30 nm. Moreover, Figure 4d-f revealed a gradual decrease in the pore size of the group-2 materials as earlier revealed in Table 1. Finally, it is inexplicably clear that the SEM images did not depict any descriptive shape of the

The EDS analyses were carried out to qualitatively determine the surface elemental components and mappings thereon the materials. The results of these analyses are shown in Figure 5. Clearly, the profiles confirmed the presence of Si  $K\alpha$  around 1.9 keV, O  $K\alpha$  around 1.5 keV, and Zr  $L\alpha$  around 2.0 keV. Some amount of carbon, C  $K\alpha$  around 0.25 keV, was also detected, from part of the carbon tape used in the measurement. Moreover, the insets revealed the presence of Ni in all the materials, Ni  $K\alpha$  was detected around 7.5 keV. It was also observable among each group of materials that as the Ni loading increased, the intensity of the Ni  $K\alpha$  peak also increased. As for the Zr  $K\alpha$  however, the intensity was broad and relatively constant as expected among the group-2 materials.

Moreover, the EDS elemental maps of the group-1 and group-2 materials are also presented, Figure 6 for the group-1 materials and Figure 7 for the group-2 materials. In both figures, Figures 6a,d,g and 7a,e,i are the representative SEM images of the samples. In the group-1 materials, the elemental maps of the Ni, Figure 6c,f,i, can be seen perfectly mapped on the corresponding silica maps, Figure 6b,e,h. Moreover, gradation in the intensity of Ni can also be seen in Figure 6c,g,i, confirming the relative number of cycles of Ni deposited on each sample in the group.

Similarly, within the group-2 materials, we could see the elemental maps of the Zr (Figure 7c,g,k) on the silica supports (Figure 7b,f,j) with excellent dispersion. However, no information about the  $ZrO_2$  film thickness could be gathered

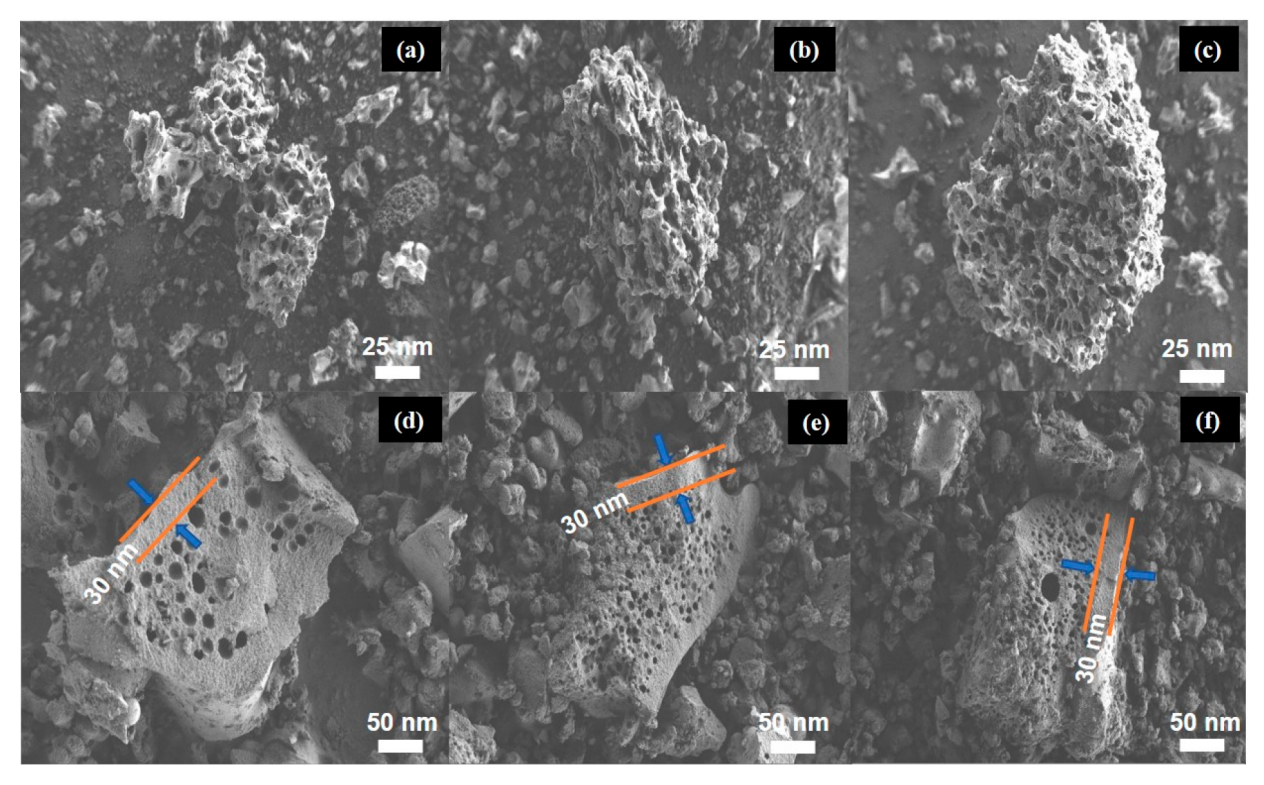


Figure 4. SEM images of (a) 1Ni/SiO<sub>2</sub> (b) 2Ni/SiO<sub>2</sub> (c) 3Ni/SiO<sub>2</sub> (d) 1Ni/ZrO<sub>2</sub>-SiO<sub>2</sub> (e) 2Ni/ZrO<sub>2</sub>-SiO<sub>2</sub> and (f) 3Ni/ZrO<sub>2</sub>-SiO<sub>2</sub>.

from this figure. As shown in Figure 7c,g,k, zirconium maps are relatively equal in intensity (brightness), thereby showing equal coating of the group-2 materials with ZrO<sub>2</sub> as earlier attested to in the XPS results. The addition of Ni on the composites ZrO<sub>2</sub>–SiO<sub>2</sub> is also observable from the accurate maps of Ni shown in Figure 7d,h,l indicating even dispersion of Ni particles across the composites. In both Figures 6 and 7, the Ni particle size was estimated to be about 3–5 nm. Moreover, gradation in the intensity of Ni could also be observed as evidence of the change in the amount of Ni deposition. In summary, as shown in the maps, both ZrO<sub>2</sub> and Ni loaded effectively on the silica support.

To quantify the surface elemental compositions and gain insight into the elemental chemical states of the materials, XPS analyses were performed. The profiles are shown in Figure 8. High-resolution deconvolution of the peaks corresponding to the Ni, O, S, and Zr atoms are shown in Figures S3-S4 Supporting Information. All of the profiles were adjusted with the adventurous C 1s peak at 284.5 eV due to observed charging effects during the XPS analyses. All of the characteristic peaks of Ni 2p were detected as shown in Figure 8a,d. Ni  $2p_{3/2}$  was detected around 855.6 eV, while its satellite counterpart was detected at 861 eV, Ni  $2p_{1/2}$  was detected at 873 eV, and its satellite counterpart at 880 eV. The satellite peaks were ascribed to shakeup electrons.36 Moreover, increases in Ni 2p peaks intensities were observed as the number of the cycles of Ni coating increased. Based on the work of Biesinger et al.,<sup>37</sup> the nickel oxidation state on the surface of the materials was estimated to be Ni<sup>2+</sup> from NiO and/or Ni(OH)2. One distinct characteristic peak of O 1s was detected at 533 eV, Figure 8b,e. Similarly, Si 2p was detected across all the materials, Figure 8c,f), at a binding energy location (103.5 eV) that had been attributed to SiO<sub>2</sub>. It was noteworthy that intensities of O 1s and Si 2p decreased with Ni loading similar to what was observed by Seo et al.<sup>35</sup> This of course was not surprising because XPS is a surface analysis tool (about 5 nm surface thickness). For the samples denoted by  $x \text{Ni/ZrO}_2 - \text{SiO}_2$ , two characteristic peaks of Zr 3d were detected, Zr  $3d_{3/2}$  and  $3d_{5/2}$  at 184 and 182 eV, respectively, corresponding with  $\text{Zr}^{4+}$ . However, there was a slight difference in the intensities of  $\text{ZrO}_2$  present in all these materials as can be seen in Figure 8g and also in Table 2.

The surface mass (%) elemental compositions of the group-1 and group-2 materials are shown in Table 2. Clearly, the amounts of O and Si were closely similar in each group of the materials thereby showing uniformity in the composition of the SiO<sub>2</sub> bare supports in each of the groups. The 0.5% N composition in Table 2 most certainly came from the (Zr(NMe2)4 precursor used during the ALD. As expected, Ni loading gradually increased with the number of ALD cycles in both groups of materials. Notably, the Ni surface loadings on the group-2 materials were found to be significantly higher than the corresponding group-1 loadings. This was because the ZrO<sub>2</sub> thin film on which Ni was deposited in the group-2 materials is nonporous as clearly shown in Figure 4, thereby restricting Ni deposition barely to the external surface.<sup>35</sup> The surface amounts of the Zr on the group-2 materials were also very similar. A similar table but based on atom (%) compositions, inclusive of the composition of the group-0 materials, is shown in Table S1 in the Supporting Information.

Determining the quantity and strength of the active sites on an adsorbent and/or catalyst is crucial to understanding and predicting the performance of the material. For this reason, NH<sub>3</sub>-TPD was carried out on each of the materials. By this, we could determine the number of desorption peaks (types of adsorption active sites), the volume of desorption (number of adsorption active sites), and the desorption temperature (activation energy of desorption). The profiles for the group-1 and group-2 materials are shown in Figure 9, while those for the group-0 materials are shown in Figure S5 in the Supporting

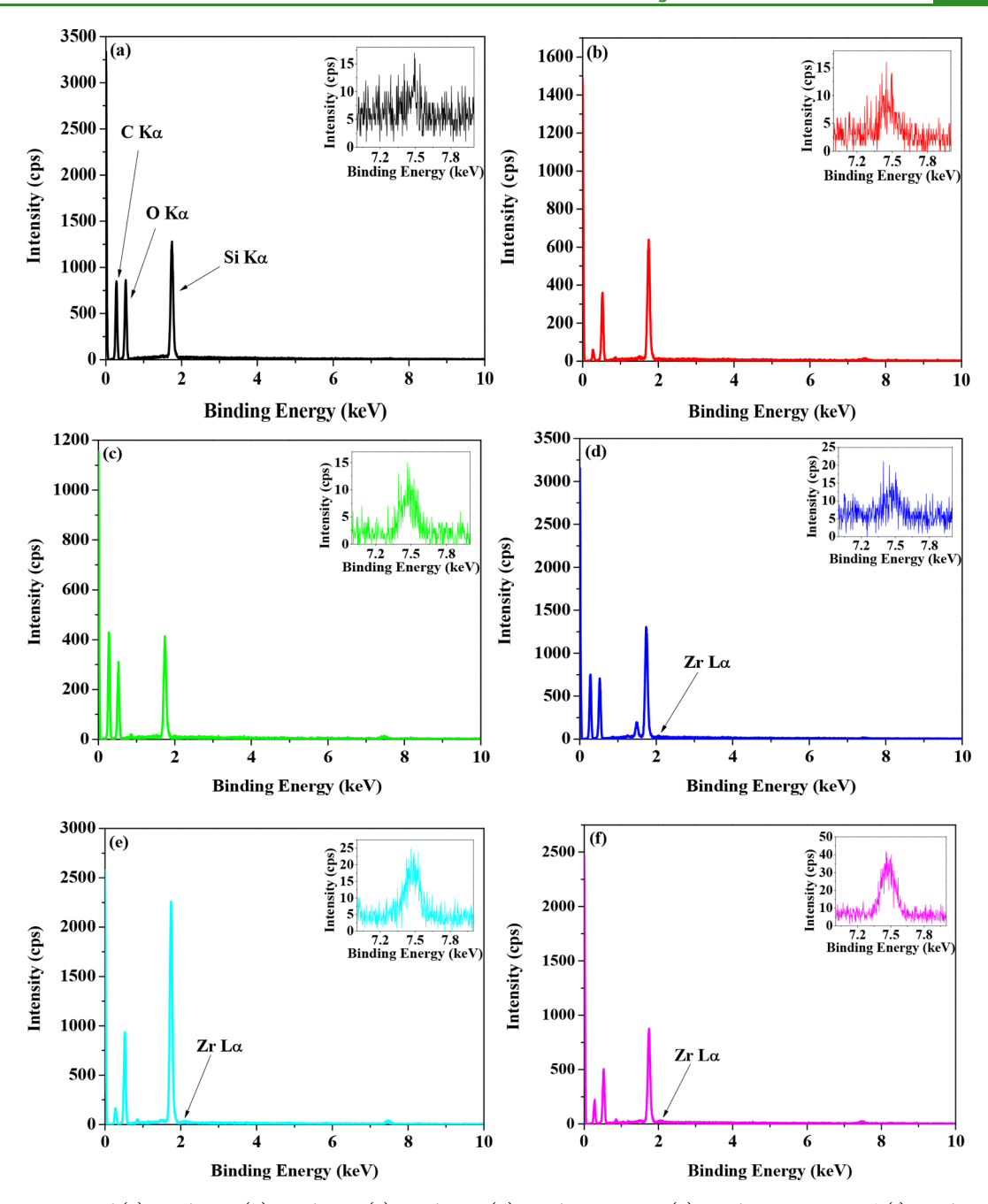


Figure 5. EDS spectra of (a)  $1Ni/SiO_2$ , (b)  $2Ni/SiO_2$ , (c)  $3Ni/SiO_2$ , (d)  $1Ni/ZrO_2-SiO_2$ , (e)  $2Ni/ZrO_2-SiO_2$ , and (f)  $3Ni/ZrO_2-SiO_2$ . The insets contain Ni  $K\alpha$ , detected around 7.5 keV.

Information. The values of the important parameters (peak temperature, area, height, and width) evaluated from the profiles are shown in Tables S2 and S3 in the Supporting Information. Peak deconvolution using Gauss function was also carried out in order to see any hidden peaks within the profiles. Generally, a low-temperature (<200 °C) peak is attributed to a physisorption site or weak acid site, a medium-temperature (200–500 °C) peak to a moderate acid site, and a high-temperature (>500 °C) peak to a strong acid site. For the bare silica material, Figure S5a in the Supporting Information revealed three peaks. The first and sharp peak, centered at 133 °C could be ascribed to physisorption sites, while the second and the third and broad peaks centered at 521 and 659 °C were for strong acid sites. However, the strong acid sites peaks formed a shoulder around 450–800 °C. Coating ZrO<sub>2</sub> on the

bare SiO<sub>2</sub>, created two weak new peaks (175 and 245 °C), while the number of strong acid sites peaks was reduced from two to one with a significant reduction in the peak desorption temperature and area. The increase in the temperature of weakest active sites peak desorption temperature from 133 to 135 °C in conjunction with the creation of the new low-temperature peaks could be tentatively ascribed to strong adsorption affinity on the ZrO<sub>2</sub>–SiO<sub>2</sub>. Though the coating of ZrO<sub>2</sub> on SiO<sub>2</sub> reduced its surface area and pore volume, as shown in Table 1, more hydroxyl (OH) groups active sites, presumably at this juncture for benzene physisorption, were created as shall be confirmed later. A similar observation was reported by Tyagi et al.<sup>38</sup> For the group-1 materials, incorporation of Ni on the silica support, though preserved its existing peaks, created a new peak centered respectively at

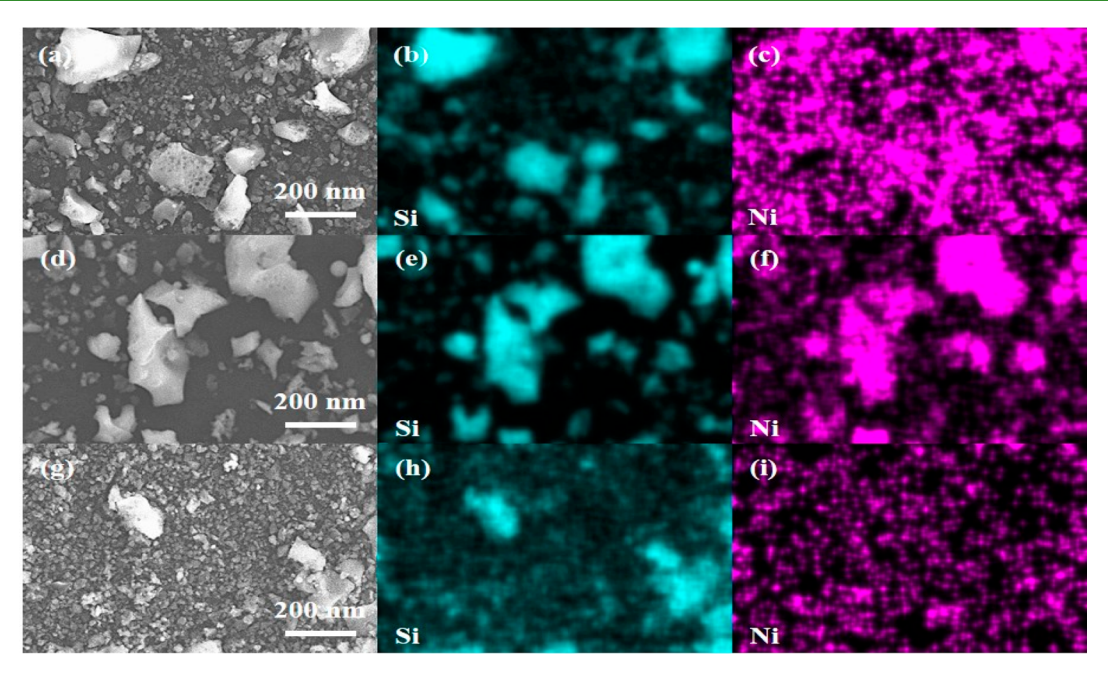


Figure 6. EDS elemental maps of (a-c) 1Ni/SiO<sub>2</sub>, (d-f) 2Ni/SiO<sub>2</sub>, and (g-i) 3Ni/SiO<sub>2</sub>.

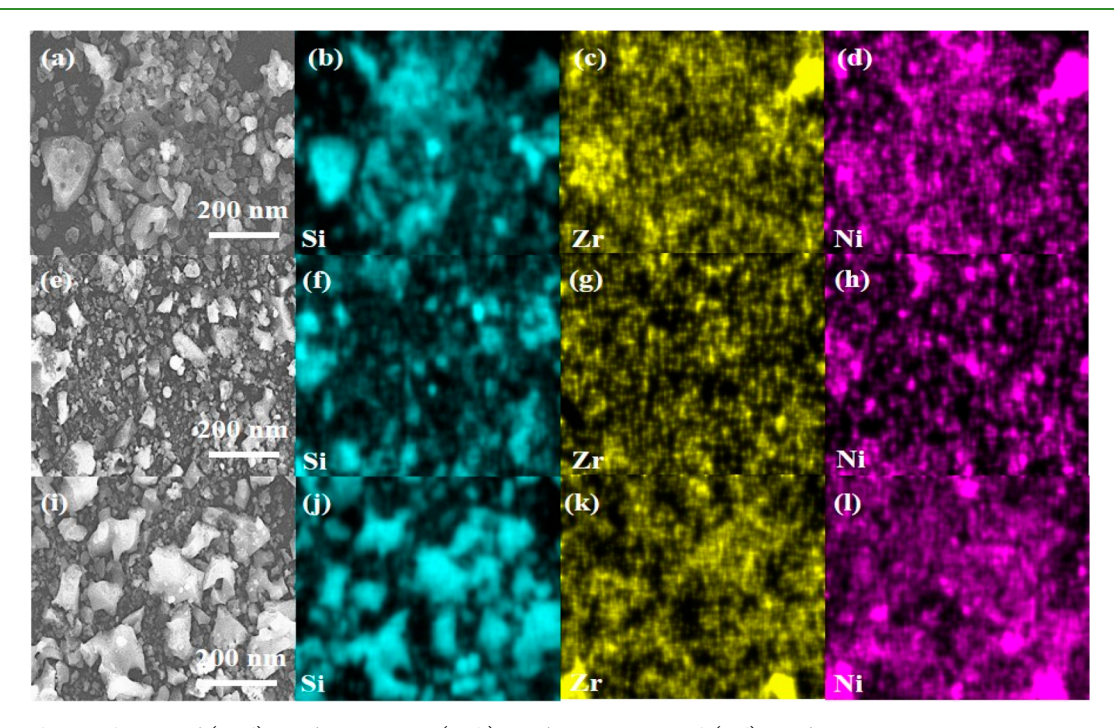


Figure 7. EDS elemental maps of (a-d) 1Ni/ZrO<sub>2</sub>-SiO<sub>2</sub>, (e-h) 2Ni/ZrO<sub>2</sub>-SiO<sub>2</sub>, and (i-l) 3Ni/ZrO<sub>2</sub>-SiO<sub>2</sub>.

183, 191, and 196 °C with a proportionate increase in peak area (11672, 18264, and 24214 ppm °C) as Ni loading increased (see Figure 9 and Table S2). This new peak, found around 180–200 °C, has been ascribed to the presence of Ni as reported by other researchers.<sup>39</sup> However, there were peak shifts, suggesting a Ni–silica interaction. It is well-known that strong-metal support interaction (SMSI) reduces adsorption. It is assumed at this point that this peak was for weak acid sites and not for physisorption sites and shall be substantiated later. Comparing the group-0 and group-1 materials, we could see that, even though the surface area and pore volume decreased with ZrO<sub>2</sub> or Ni loadings, more active sites were created either to boost physical adsorption (ZrO<sub>2</sub> active sites) or enhance

catalysis (Ni active sites). For the group-2 materials, it is interesting that the same number of peaks and desorption temperature ranges were detected as were in the group-1 materials. However, as Ni loading increased, desorption temperature gradually increased in all of the peaks, while the peak area gradually increased in the first three peaks but decreased in the last and strongest one. The relative measure of the number of active sites in each material denotes the total area under the NH<sub>3</sub>-TPD profile. The total area under these peaks for each material can be found in Table S2 in the Supporting Information. It is believed that this resultant trend correlated with the overall activity of the materials measured by TOF as shall be validated later. Among the group-1 materials,

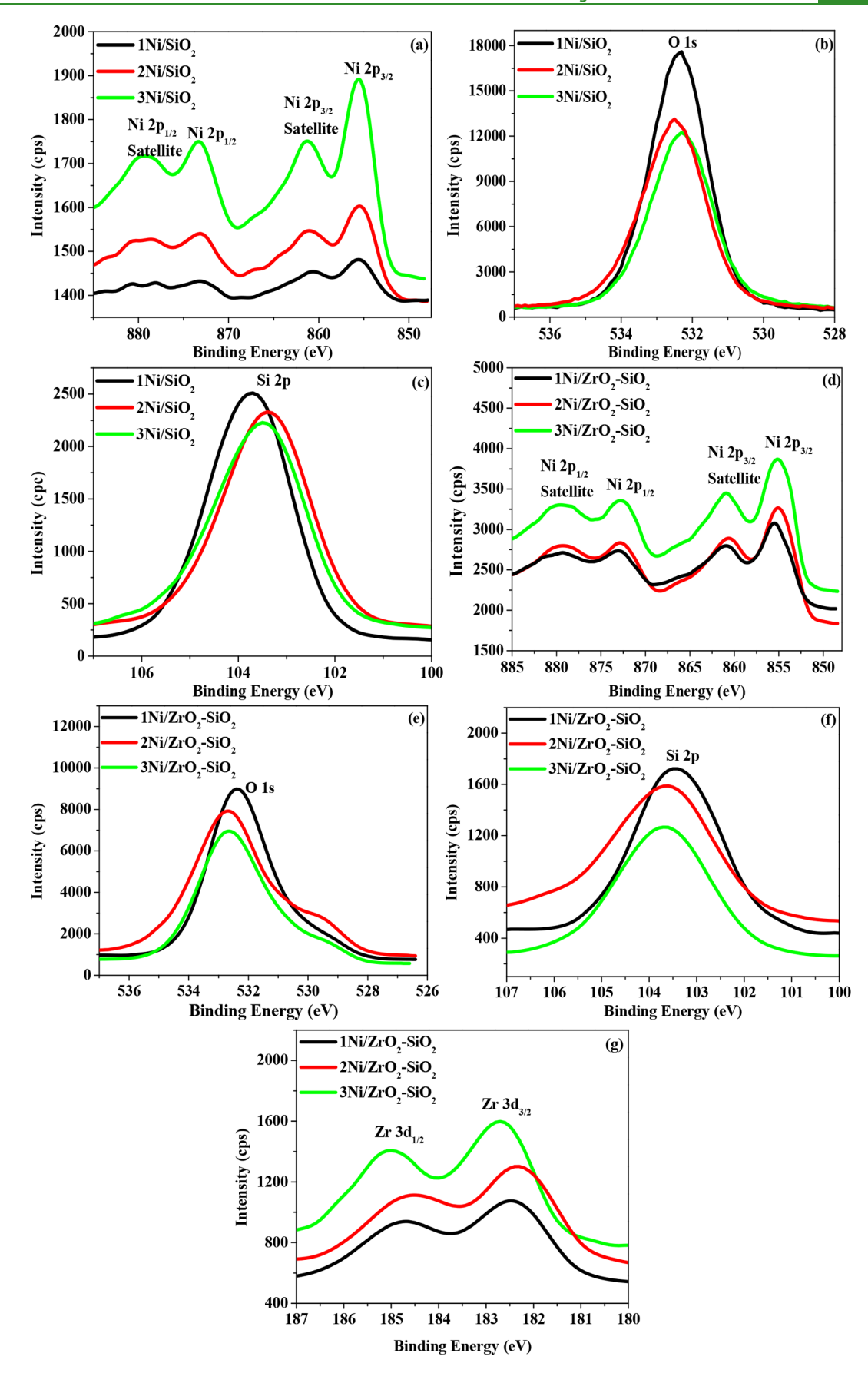


Figure 8. XPS spectra of  $(a-c) \times Ni/SiO_2$  and  $(d-g) \times Ni/ZrO_2 - SiO_2$ .

Table 2. Mass (%) Surface Elemental Compositions of the Samples Determined by XPS

sample	Si mass (%)	O mass (%)	N mass (%)	C mass (%)	Ni mass (%)	Zr mass (%)
1Ni/SiO <sub>2</sub>	41.4	55.6	-	1.4	1.5	-
2Ni/SiO <sub>2</sub>	39.4	53.5	-	2.6	4.4	-
3Ni/SiO <sub>2</sub>	38.3	50.3	-	3.8	7.6	-
$1 \text{Ni}/\text{ZrO}_2 - \text{SiO}_2$	23.7	42.3	0.5	11.7	14.5	7.3
$2Ni/ZrO_2-SiO_2$	22.9	39.9	0.5	10.6	18.3	7.8
$3Ni/ZrO_2-SiO_2$	21.1	39.3	0.5	10.0	20.8	8.3

peak width increased as Ni loading increased in peaks 1, 2, and 4 but decreased in peak 3. The peak width is a measure of the active site strength.

**3.2. Benzene Vapor Adsorption Isotherms.** The results of the benzene vapor adsorption isotherm measurements are shown in Figure 10, while that of the bare silica is shown in Figure S6 in the Supporting Information. Similar to the  $N_2$  physisorption isotherms, the benzene vapor adsorption isotherms clearly depicted the type IV isotherm according to the IUPAC classification. A critical parameter in the assessment of adsorbent applicability is the kinetic diameter of the adsorptive relative to the adsorbent pore diameter, the

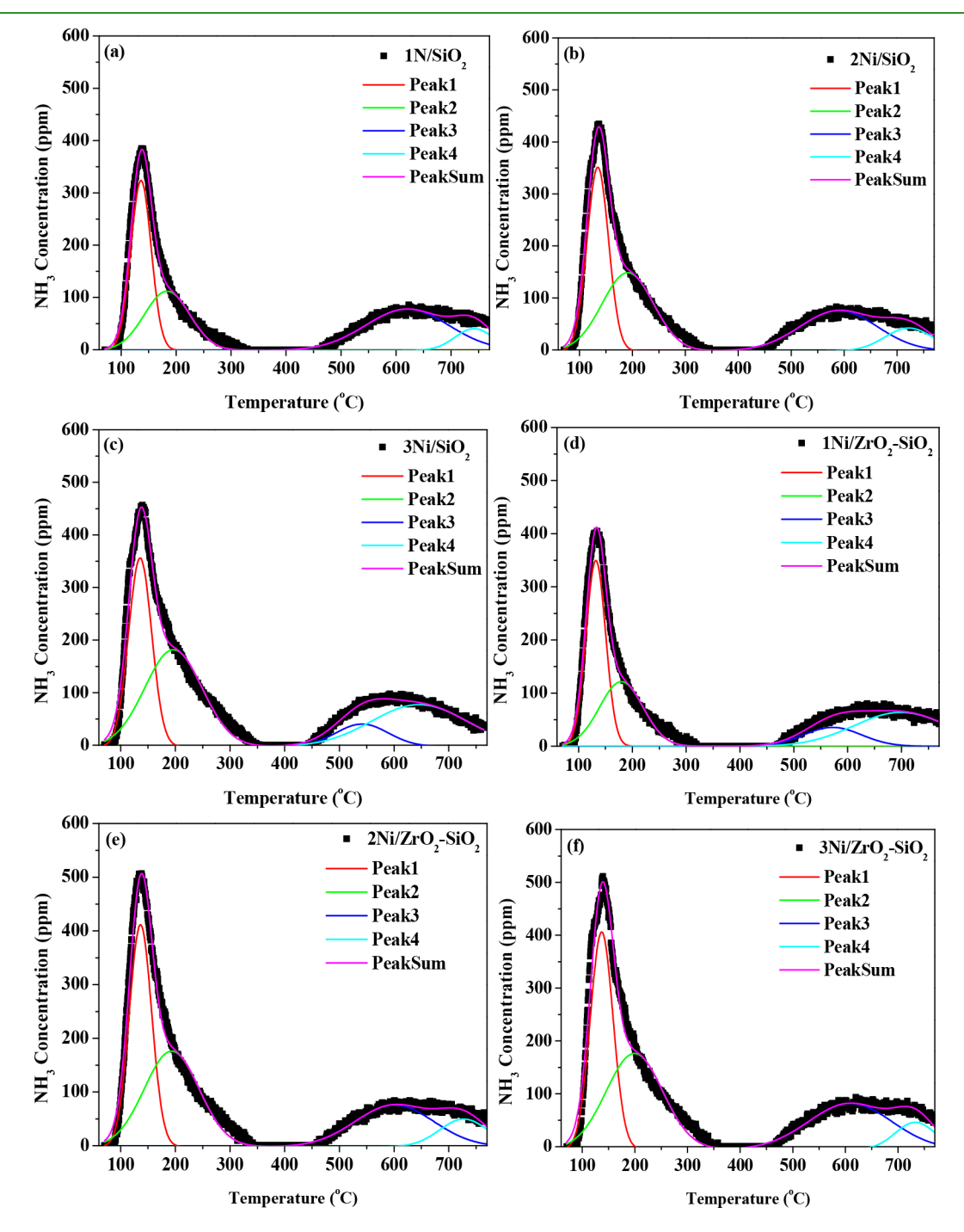


Figure 9. NH<sub>3</sub>-TPD profiles of (a-c) xNi/SiO<sub>2</sub> and (d-f) xNi/ZrO<sub>2</sub>-SiO<sub>2</sub> from 80 to 800 °C.

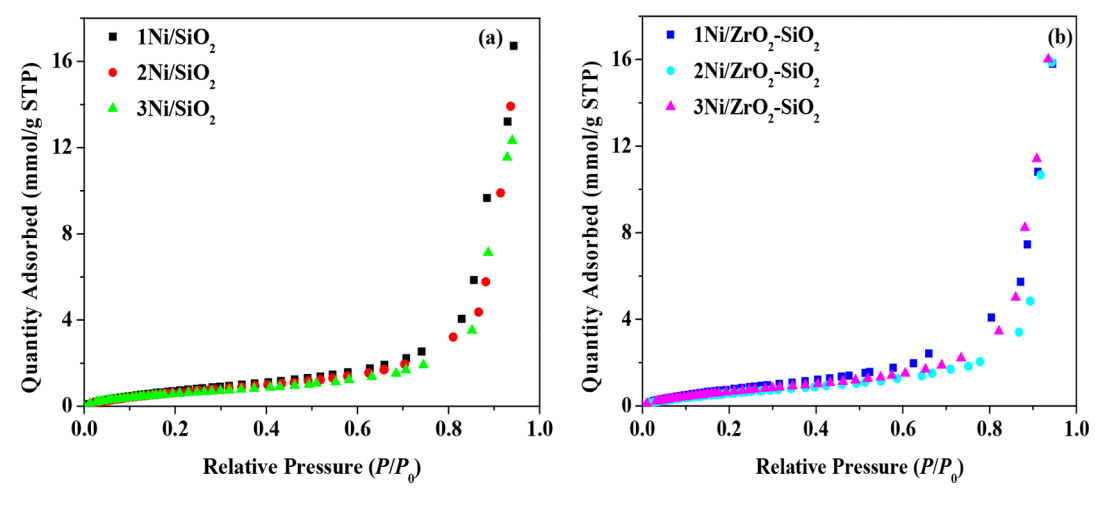


Figure 10. Benzene vapor isotherms of (a) xNi/SiO<sub>2</sub> and (b) xNi/ZrO<sub>2</sub>-SiO<sub>2</sub>.

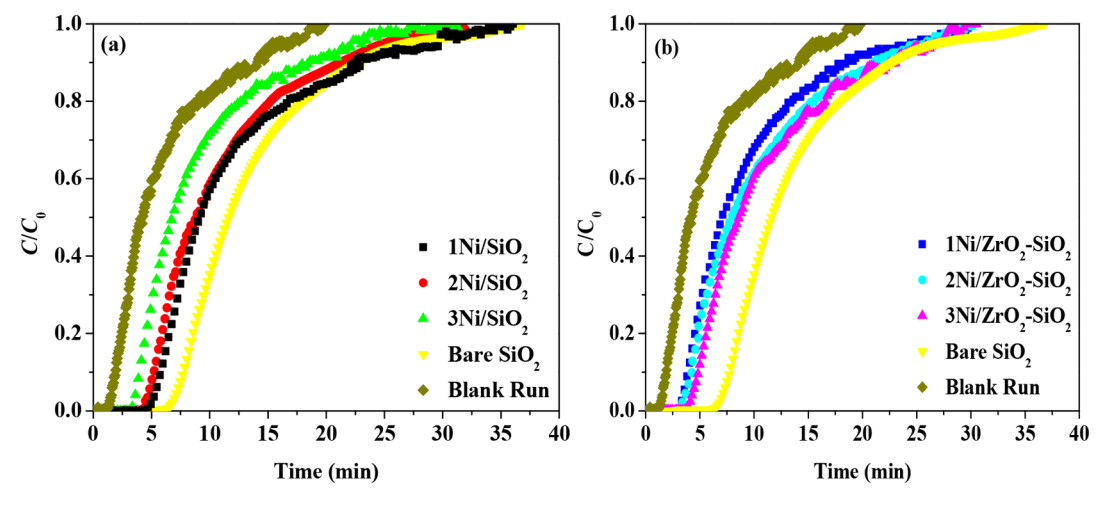


Figure 11. Benzene vapor breakthrough profiles of (a) xNi/SiO<sub>2</sub> and (b) xNi/ZrO<sub>2</sub>-SiO<sub>2</sub>.

value of which for benzene is about 5.9 Å. This implies that all the materials investigated in this work, with the pore diameters shown in Table 1, have sufficiently large pores for the benzene diffusion without any intraparticle diffusional resistance. The isotherms in Figure 10 clearly show three consecutive stages of adsorption: monolayer adsorption, multilayer adsorption, and capillary condensation. Across all the materials, the end of the monolayer adsorption and beginning of multilayer adsorption was about  $P/P_0$  < 0.25, while the end of the multilayer adsorption and beginning of capillary condensation was about  $P/P_0 > 0.80$ . As shown in Figure 10a, we can see that the equilibrium adsorption uptake decreased with Ni loading among the group-1 materials, in particular over the medium and high relative pressure range. For instance, with 1Ni/SiO<sub>2</sub> having an equilibrium adsorption uptake of 16.7 mmol/g STP as the relative pressure approached the benzene saturation vapor pressure, i.e.,  $P/P_0 \rightarrow 1$ ,  $2Ni/SiO_2$  suffered a 17% decrease compared to 1Ni/SiO2, 3Ni/SiO2 experienced a 12% decrease compared to 2Ni/SiO<sub>2</sub>, and 3Ni/SiO<sub>2</sub> underwent a 26% decrease compared to 1Ni/SiO<sub>2</sub>. This observation can be explained from two different perspectives: (i) decrease in surface area and (ii) loss of surface OH groups via SMSI.<sup>20,35</sup> For the group-2 materials, it is interesting to see how the two main equilibrium-adsorption-capacity-determinants (surface area and OH groups) played out. At  $P/P_0$  < 0.85, 1Ni/

ZrO<sub>2</sub>-SiO<sub>2</sub> depicted the highest benzene uptake due to its highest number of OH groups, followed by 3Ni/ZrO2-SiO2 due to its highest surface area. Beyond this point and as  $P/P_0$ → 1, it is observable that 3Ni/ZrO<sub>2</sub>-SiO<sub>2</sub> has the highest benzene uptake because of its superior surface area among the group-2 materials. Given the greater slope of the adsorption isotherm of  $2Ni/ZrO_2$ -SiO<sub>2</sub> as  $P/P_0 \rightarrow 1$ , it is clear that the equilibrium adsorption capacity at this point was also greater than that of 1Ni/ZrO2-SiO2. Thus, it is conclusive that the equilibrium adsorption uptake of the group-2 materials increased with Ni loading as  $P/P_0 \rightarrow 1$ . It is worth mentioning that the ZrO2-SiO2 has the largest equilibrium adsorption uptake as revealed in Figure S6 in the Supporting Information basically due to its high number of surface OH groups.<sup>4</sup> Moreover, it should be pointed out that the gradual change in equilibrium uptake observed among these materials could be due to the small difference in the number of cycles of Ni ALD on these materials.<sup>41</sup> Overall, all the materials depicted a relatively large adsorption uptake, close to the benzene saturation vapor pressure (average of 16 and 15 mmol/g for group-1 and group-2 materials, respectively), thereby suggesting these materials are excellent materials for concentrating of benzene vapor before catalytic oxidation.

**3.3. Dynamic Adsorption Breakthrough Profiles.** The results of the benzene vapor dynamic adsorption experiments

Table 3. Material Dynamic Adsorption Data Obtained from Breakthrough Profiles

sample	$t_{0.05}$ (min)	$t_{1.0}$ (min)	$t_{\rm s}~({\rm min})$	MTZ (min)	$q_{\rm d,0.05}~(\rm mmol/g)$	$q_{\rm d,1.0}~(\rm mmol/g)$	$q_{\rm d,s}~({\rm mmol/g})$	$q_{\rm eq} \ ({\rm mmol/g})$
Bare SiO <sub>2</sub>	5.6	17.0	13.6	11.4	3.2	9.7	7.8	18.9
ZrO <sub>2</sub> -SiO <sub>2</sub>	7.5	24.5	19.7	17.0	4.3	14.0	11.2	25.1
1Ni/SiO <sub>2</sub>	3.8	16.2	12.1	12.4	2.1	9.2	6.8	16.7
2Ni/SiO <sub>2</sub>	3.2	12.1	11.6	8.9	1.8	6.9	6.3	15.3
3Ni/SiO <sub>2</sub>	2.3	9.0	9.3	6.7	1.3	5.1	5.1	13.9
$1 \text{Ni}/\text{ZrO}_2 - \text{SiO}_2$	2.0	10.2	9.5	8.2	1.1	5.8	5.4	15.8
$2Ni/ZrO_2-SiO_2$	2.2	10.3	10.4	8.1	1.2	5.9	5.9	15.9
$3Ni/ZrO_2-SiO_2$	2.8	10.8	11.1	8.0	1.6	6.2	6.3	16.1

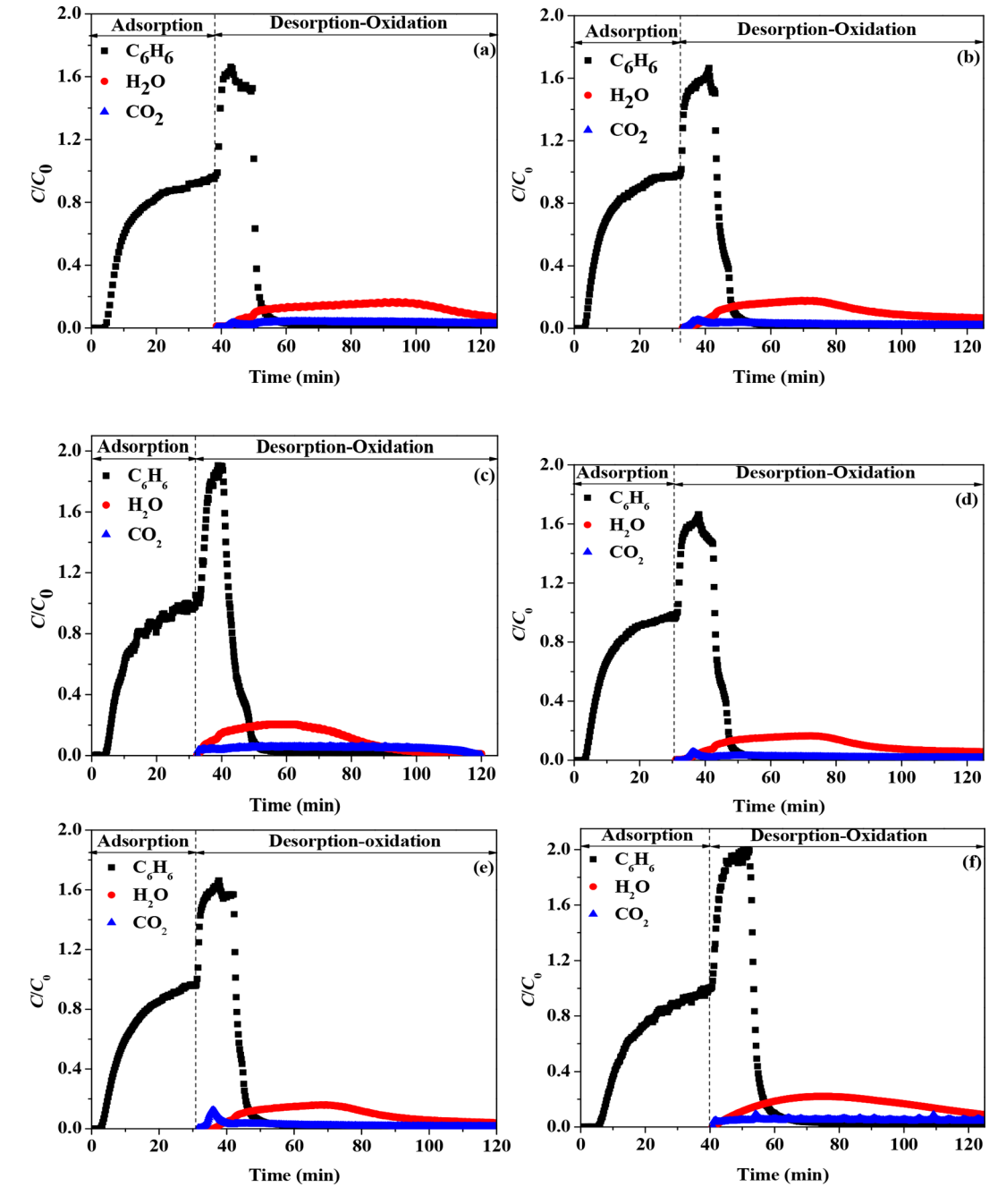


Figure 12. Adsorption-reaction profiles of (a)  $1Ni/SiO_2$ , (b)  $2Ni/SiO_2$ , (c)  $3Ni/SiO_2$ , (d)  $1Ni/ZrO_2-SiO_2$ , (e)  $2Ni/ZrO_2-SiO_2$ , and (f)  $3Ni/ZrO_2-SiO_2$ .

carried out on the group-1 and group-2 materials together with that on the bare SiO<sub>2</sub> are shown in Figure 11, while that on the

ZrO<sub>2</sub>-SiO<sub>2</sub> together with that on the bare SiO<sub>2</sub> is shown in Figure S7 in the Supporting Information. The blank run result

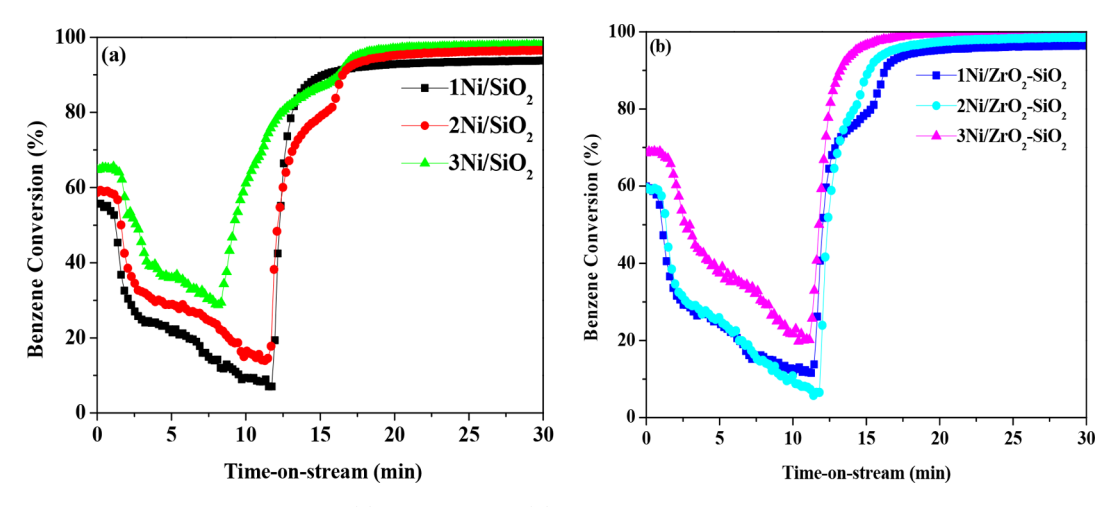


Figure 13. Benzene instantaneous conversion of (a) xNi/SiO<sub>2</sub> and (b) xNi/ZrO<sub>2</sub>-SiO<sub>2</sub>.

was included in Figure 11 to show the hydrodynamics of benzene in the empty column. It should be mentioned first that the results were all in trend with the equilibrium adsorption results at the benzene saturated vapor pressure. Among the group-1 materials, we can see that breakthrough and saturation times decreased gradually with Ni loading. Generally, the factors that are responsible for these times in dynamic adsorption are materials textural and surface properties (pore size and volume, surface area, charge/polarity, roughness, and functional groups), bed porosity, length (weight) and inlet conditions (pressure/concentration and temperature). 42,43 In as much as our dynamic experiments were all carried out under the same bed weight and inlet conditions, and with a reasonable assumption that the beds of the materials all had similar porosity, then we can rule out possible effects of those factors on the characteristic times. This then left us with using the remaining factor, i.e., material properties, as the determinants of those times. Hence, it is assertive that the same reasons that were responsible for the trends in equilibrium adsorption uptakes were also responsible for the trends observed herein for the breakthrough and saturation times.

The summary of the key parameters calculated from the breakthrough profiles is shown in Table 3. For comparison, the equilibrium adsorption capacities were also included. As indicated in the table, among the group-1 materials, 1Ni/  $SiO_2$  showed the longest 5% breakthrough time  $(t_{0.05})$  at 3.8 min, 2Ni/SiO<sub>2</sub> at 3.2 min, and 3Ni/SiO<sub>2</sub> at 2.3 min. This performance is relatable to the number of Ni coatings in a way such that an increase in Ni coating caused pore blockage of the porous SiO<sub>2</sub> support and hence the characteristic times. A similar trend was also observed in the 100% breakthrough, i.e., saturation time  $(t_{1.0})$  and likewise the stoichiometric time  $(t_s)$ . As the increase in the number of Ni active sites (as seen in the NH<sub>3</sub>-TPD profiles) did not improve physical adsorption, then it is reasonable that the trend observed here was due to the surface properties, i.e., OH groups, surface area, and pore volume as similarly reported by Ncube et al.40 However, the group-2 materials showed an increase in those characteristic times as shown in Table 3. This trend observed in the group-2 materials could be linked to a synergy between high surface area and increased OH groups. 44 All of this could be translated into a progressive decrease and increase in dynamic adsorption capacity in group-1 and group-2 materials respectively with Ni

loading. The temporal values of the mass transfer zone (MTZ  $= t_{1.0} - t_{0.05}$ ) decreased from 12.4 min (1Ni/SiO<sub>2</sub>) to 8.9 min (2Ni/SiO<sub>2</sub>) to 6.7 min (3Ni/SiO<sub>2</sub>) compared to 8.2, 8.1, and 8.0 min for the 1Ni/ZrO<sub>2</sub>-SiO<sub>2</sub>, 2Ni/ZrO<sub>2</sub>-SiO<sub>2</sub>, and 3Ni/ ZrO<sub>2</sub>-SiO<sub>2</sub> materials, respectively. The shape and the size of the MTZ usually depend on the adsorption isotherm (universally characterized by the adsorption affinity), flow rate, and the mass transfer rate. In as much as we used same flow rate for the dynamic adsorption experiments across all the materials and that the materials' pores have similar sizes and distributions (as seen in Table 1), we can conclude that the temporal values of the MTZ zone in this study were primarily dictated by the adsorption affinity. The adsorption affinities calculated in Henry's low-pressure region for the group-1 and group-2 materials were 5.00, 4.75, 4.70, 4.55, 4.65, 4.75 mmol/ g STP. As we can see, the higher the adsorption affinity, the shorter is the MTZ value and vice versa. Unexpectedly, the dynamic stoichiometric adsorption capacity was lower than the corresponding steady-state equilibrium adsorption capacity. As expected, the values of  $t_{1.0}$  and  $t_{s}$  and thus  $q_{d,1.0}$ , and  $q_{d,s}$  were significantly close because they were two different measures of similar parameters (adsorption time and adsorption quantity, respectively). However, the dynamic adsorption capacities  $(q_d)$ were significantly different from the equilibrium adsorption capacities  $(q_{eq})$ . The difference observed in these values could be attributed to a few factors such as improper and/or unsaturated vapor generation used for the dynamic adsorption experiments. Mokhatab et al.<sup>45</sup> showed that the dynamic adsorption capacity is usually about 50-70% of the equilibrium adsorption capacity.

# **3.4. Combined Adsorption-Reaction Performances.** Catalytic oxidation was carried out on the group-1 and group-2 materials in order to assess their catalytic performance and their ease of oxidative regeneration. For these materials, benzene desorption was first detected at about 90 °C. The desorbed benzene was subsequently reacted with oxygen in the feed stream of $79/21-N_2/O_2$ air at a flow rate of 10 mL/min to yield $CO_2$ and $H_2O$ . The results of the sequential adsorption and catalytic oxidation experiments are shown in Figure 12. First and foremost, it is pertinent to mention that only the profiles of $C_6H_6$ , $CO_2$ , and $H_2O$ are shown in Figure 12 because $O_2$ and $N_2$ were well in excess during the catalytic oxidation. It is noticeable in these profiles that the transition from adsorption to desorption cum catalytic oxidation started

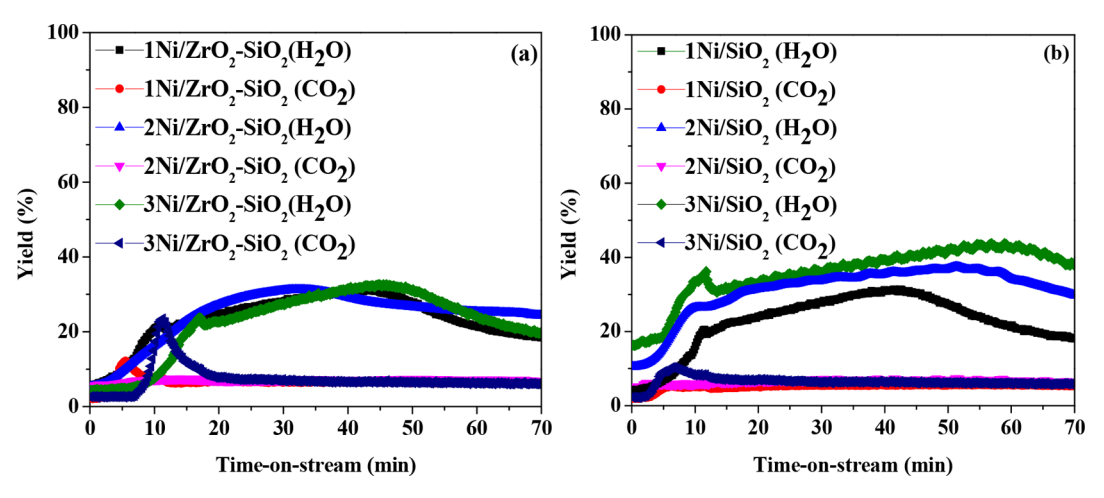


Figure 14. Reaction products' yields of (a) xNi/SiO<sub>2</sub> and (b) xNi/ZrO<sub>2</sub>-SiO<sub>2</sub>.

Table 4. Benzene Oxidation Performance Variables (TOF, Conversion, Yield, and Selectivity)

sample	$reaction\ TOF\ (mmol_{C6H6}/mol_{Ni}/s)$	C <sub>6</sub> H <sub>6</sub> conversion (%)	H <sub>2</sub> O yield (%)	CO <sub>2</sub> yield (%)	H <sub>2</sub> O selectivity (%)	CO <sub>2</sub> selectivity (%)
1Ni/SiO <sub>2</sub>	1.28	85	25	5	27	4.7
2Ni/SiO <sub>2</sub>	1.29	88	25	6	34	4.5
3Ni/SiO <sub>2</sub>	1.31	91	23	8	26	5.6
$1 \text{Ni/ZrO}_2 - \text{SiO}_2$	2.86	90	23	4	28	5.5
$2Ni/ZrO_2-SiO_2$	5.53	92	30	4	27	6.5
$3Ni/ZrO_2-SiO_2$	16.42	96	39	5	24	8.3

with initial roll-ups above  $C/C_0 \approx 1$ . These initial roll-ups were due to the net positive inter/intraparticle gas-phase concentration of benzene at the end of saturation adsorption, and the difference between the amount desorbed and the amount oxidized. As can be seen in Figure 12, benzene concentration started decreasing shortly after the roll-up attained the climax due to the fact that the inter/intraparticle gas-phase concentration of benzene at the end of saturation adsorption had been completely pushed out of the bed or otherwise reacted while the rate of desorption was still greater than the rate of oxidation. Therefore, the excess of desorption over oxidation was the benzene detection. Approximately about 15-20 min after the roll-up climax, complete oxidation of desorbed benzene was achieved as can be seen in the profiles. We could see that the benzene oxidation rate increased gradually with Ni loading in both groups of materials evidenced by the proportionate decrease in the time to complete reaction. Moreover, it is remarkable that the amount of H<sub>2</sub>O produced was higher (almost 50%) than that of CO<sub>2</sub>, a sharp contrast to the reaction stoichiometry of benzene oxidation as written in eq S6 in the Supporting Information. This could be a consequence of possible high-temperature readsorption of the produced CO<sub>2</sub> on the materials. Also noticeable in Figure 12 is that, for all of the materials, desorption kinetics were faster than adsorption kinetics as revealed by the slope of each step. This was not unexpected as pore blockage tends to increase as adsorption progresses therefore causing a barrier to fast diffusion within the materials' pores.3

For these materials, the time-on-stream (instantaneous) conversion during the catalytic oxidation of the thermally desorbed benzene was calculated and the results are shown in Figure 13. For the group-1 materials, as Ni loading increased, initial conversion was about 59, 61, and 65%, but thereafter conversion decreased steadily to about 10, 15, and 30% over a

period of 12, 11, and 7.8 min, respectively. The decrease in conversion observed during this period was due to the initial roll-up when the desorption rate was greater than the oxidation rate as seen in Figure 12. It is well-known that thermal desorption is a fast and step process while oxidation is a controlled process, thereby shedding light on the decrease in conversion during the roll-up period.<sup>4</sup> It can be seen that conversion increased sharply with time after the roll-up stage. Moreover, throughout the catalytic oxidation step, conversion increased with Ni loading for both groups of materials. It is remarkable that the instantaneous conversion was already as high as 95% within 25 min of the reaction, and increased to attain 100% as the reaction proceeded to completion. This pattern of reaction conversion was reported by Rostami et al.<sup>46</sup>

Similarly, instantaneous CO2 and H2O yields were calculated and the results are shown in Figure 14. The group-1 materials showed nearly similar H<sub>2</sub>O yield over the entire reaction time, while CO2 instantaneous yield initially increased with Ni loading up until about 10 min of the reaction but later became fairly constant until the reaction completion. However, among the group-2 materials, H<sub>2</sub>O instantaneous yield increased with Ni loading, while the CO<sub>2</sub> yield followed a similar trend as was seen among the group-1 materials. Expectedly, this followed a similar trend saw in the reaction profiles of Figure 13. However, the observation could be due to a concerted effort between Ni and ZrO2. It is noteworthy to mention that CO2 yields were very small and fairly constant after 20 min of the reaction compared to the H<sub>2</sub>O yield across all materials. Moreover, similar trends were observed among the two groups of materials.

The summary of the reaction overall performance is shown in Table 4. As shown, the reaction conversion increased with Ni and/or ZrO<sub>2</sub> loadings. For instance, within the group-1 materials, there was about a 5% increase in conversion as the Ni loading increased from 1 ALD cycle to 3 ALD cycles. A

similar trend was also observed within the group-2 materials where an increase of about 6% was observed. As has been shown before, adsorption of benzene was enhanced by the ZrO<sub>2</sub> in the group-2 materials, thereby increasing the catalytic ability of the group-2 materials compare to group-1 materials. Hence, it is conclusive that both Ni and ZrO2 were essential for the higher conversions observed. The overall yields and selectivities followed the same trends seen in the instantaneous values. Using the catalytic reaction activity and the moles of the Ni present in the materials as the catalytic oxidation active species, the TOF values were calculated, and the results are included in Table 4. For these calculations, we used the values of the diameter (estimated from the EDS profiles) and dispersion (calculated using eq S15 in the Supporting Information) of the Ni particles. We could see that the TOF increased with Ni loading across the group-1 and group-2 materials in agreement with the reaction conversion. In the NH<sub>3</sub>-TPD profiles, peak 2 in the group-1 and group-2 materials was assigned to Ni active sites with areas shown in Table S2 in the Supporting Information. The trend observed in these areas correlated well with that in the benzene conversions and TOFs, i.e., as the peak area increased, conversion and TOF similarly increased. This trend, however, was not surprising for TOF is just another measure of reaction activity albeit based on the actual active species, which here were the Ni particles. The values of the TOF for the group-1 materials are in excellent agreement with the values reported in the work of Wang et al.

# 4. CONCLUSIONS

Porous SiO2 was decorated with Ni nanoparticles and/or ultrathin ZrO2 film via the ALD method. The materials were characterized and then tested for benzene adsorption at room temperature and subsequent catalytic oxidation in air at 250 °C. Benzene vapor equilibrium adsorption revealed type IV isotherm in all the materials. Moreover, equilibrium uptake decreased with loading among the group-1 (xNi/SiO<sub>2</sub>) materials but increased with loading among the group-2 (xNi/ZrO<sub>2</sub>-SiO<sub>2</sub>) materials. Similarly, the benzene vapor dynamic adsorption revealed a large uptake capacity up to about 7.5 mmol/g and fast adsorption kinetics. Successive adsorption and catalytic oxidation performed on the materials revealed their potential as dual-functional materials for the destruction of benzene. Results revealed that the total conversion of benzene increased with both Ni and ZrO2 loadings ranging from 85 to 96%. Moreover, among all of the materials, a higher H2O yield was observed compared to that of CO<sub>2</sub>. Overall, the findings of this investigation highlight the potential of novel ALD-prepared xNi/ZrO2-SiO2 as efficient dual-functional materials for application in VOC abatement processes.

# ASSOCIATED CONTENT

#### Supporting Information

The Supporting Information is available free of charge at https://pubs.acs.org/doi/10.1021/acsami.0c11666.

XPS spectra of bare SiO<sub>2</sub>, N<sub>2</sub>-physisorption isotherms of bare SiO<sub>2</sub> and ZrO<sub>2</sub>–SiO<sub>2</sub>, high-resolution XPS profiles peak deconvolution of xNi/SiO<sub>2</sub> and xNi/ZrO<sub>2</sub>–SiO<sub>2</sub>, NH<sub>3</sub>-TPD profiles of bare SiO<sub>2</sub> and ZrO<sub>2</sub>–SiO<sub>2</sub>, benzene vapor adsorption isotherm of bare SiO<sub>2</sub>, benzene breakthrough profiles of bare SiO<sub>2</sub> and

ZrO<sub>2</sub>–SiO<sub>2</sub>, atom (%) surface elemental composition of the samples determined by XPS, NH<sub>3</sub>-TPD peak temperatures and areas, NH<sub>3</sub>-TPD peak widths and heights, dynamic adsorption capacity calculation, and conversion, yield, selectivity, and TOF calculation (PDF)

# AUTHOR INFORMATION

# **Corresponding Author**

Fateme Rezaei — Department of Chemical & Biochemical Engineering, Missouri University of Science and Technology, Rolla, Missouri 65409, United States; ⊚ orcid.org/0000-0002-4214-4235; Email: rezaeif@mst.edu

#### **Authors**

- Busuyi O. Adebayo Department of Chemical & Biochemical Engineering, Missouri University of Science and Technology, Rolla, Missouri 65409, United States
- Kyle Newport Department of Chemical & Biochemical Engineering, Missouri University of Science and Technology, Rolla, Missouri 65409, United States
- Han Yu Department of Chemical & Biochemical Engineering, Missouri University of Science and Technology, Rolla, Missouri 65409, United States
- Ali A. Rownaghi Department of Chemical & Biochemical Engineering, Missouri University of Science and Technology, Rolla, Missouri 65409, United States; orcid.org/0000-0001-5228-5624
- Xinhua Liang Department of Chemical & Biochemical Engineering, Missouri University of Science and Technology, Rolla, Missouri 65409, United States

Complete contact information is available at: https://pubs.acs.org/10.1021/acsami.0c11666

#### Notes

The authors declare no competing financial interest.

# ACKNOWLEDGMENTS

The authors thank the National Science Foundation (NSF CBET-1802049) for financially supporting this project.

#### REFERENCES

- (1) Liaud, C.; Nguyen, N. T.; Nasreddine, R.; Le Calvé, S. Experimental Performances Study of a Transportable GC-PID and Two Thermo-Desorption Based Methods Coupled to FID and MS Detection to Assess BTEX Exposure at Sub-Ppb Level in Air. *Talanta* **2014**, *127*, 33–42.
- (2) Gelles, T.; Krishnamurthy, A.; Adebayo, B.; Rownaghi, A.; Rezaei, F. Abatement of Gaseous Volatile Organic Compounds: A Material Perspective. *Catal. Today* **2020**, *350*, 3–18.
- (3) Krishnamurthy, A.; Adebayo, B.; Gelles, T.; Rownaghi, A.; Rezaei, F. Abatement of Gaseous Volatile Organic Compounds: A Process Perspective. *Catal. Today* **2020**, *350*, 100–119.
- (4) Kullavanijaya, E.; Trimm, D. L.; Cant, N. W. Adsocat: Adsorption/Catalytic Combustion for VOC and Odour Control. *Stud. Surf. Sci. Catal.* **2000**, *130*, 569–574.
- (5) Kullavanijaya, E.; Cant, N. W.; Trimm, D. L. The Treatment of Binary VOC Mixtures by Adsorption and Oxidation Using Activated Carbon and a Palladium Catalyst. *J. Chem. Technol. Biotechnol.* **2002**, 77 (4), 473–480.
- (6) Nikolajsen, K.; Kiwi-Minsker, L.; Renken, A. Structured Fixed-Bed Adsorber Based on Zeolite/Sintered Metal Fibre for Low Concentration VOC Removal. *Chem. Eng. Res. Des.* **2006**, 84 (7), 562–568.

- (7) Wang, Y.; Yang, D.; Li, S.; Chen, M.; Guo, L.; Zhou, J. Ru/ Hierarchical HZSM-5 Zeolite as Ef Fi Cient Bi-Functional Adsorbent/Catalyst for Bulky Aromatic VOCs Elimination. *Microporous Mesoporous Mater.* **2018**, 258, 17–25.
- (8) Kolade, M. A.; Kogelbauer, A.; Alpay, E. Adsorptive Reactor Technology for VOC Abatement. *Chem. Eng. Sci.* **2009**, *64* (6), 1167–1177.
- (9) Yanyan, L.; Kurniawan, T. A.; Zhu, M.; Ouyang, T.; Avtar, R.; Dzarfan Othman, M. H.; Mohammad, B. T.; Albadarin, A. B. Removal of Acetaminophen from Synthetic Wastewater in a Fixed-Bed Column Adsorption Using Low-Cost Coconut Shell Waste Pretreated with NaOH, HNO<sub>3</sub>, Ozone, and/or Chitosan. *J. Environ. Manage.* **2018**, 226, 365–376.
- (10) Barea, E.; Montoro, C.; Navarro, J. A. R. Toxic Gas Removal-Metal-Organic Frameworks for the Capture and Degradation of Toxic Gases and Vapours. *Chemical Society Reviews*; Royal Society of Chemistry: London, 2014; pp 5419–5430.
- (11) Bahri, M.; Haghighat, F.; Kazemian, H.; Rohani, S. A Comparative Study on Metal Organic Frameworks for Indoor Environment Application: Adsorption. *Chem. Eng. J.* **2017**, *313*, 711–723
- (12) Ushiki, I.; Kikuchi, K.; Sato, Y.; Ito, Y.; Takishima, S.; Inomata, H. Adsorption Equilibria of VOCs (n-Octane, Propylene Glycol Monomethyl Ether, Ethanol, and 2-Propanol) on Activated Carbon under Supercritical Carbon Dioxide Conditions. *Fluid Phase Equilib.* **2018**, 462, 59–64.
- (13) Liotta, L. F. Catalytic Oxidation of Volatile Organic Compounds on Supported Noble Metals. *Appl. Catal., B* **2010**, *100* (3–4), 403–412.
- (14) Kamal, M. S.; Razzak, S. A.; Hossain, M. M. Low Temperature Catalytic Oxidation of Volatile Organic Compounds: A Review. *Atmos. Environ.* **2016**, *140*, 117–134.
- (15) Kim, H. S.; Kim, T. W.; Koh, H. L.; Lee, S. H.; Min, B. R. Complete Benzene Oxidation over Pt-Pd Bimental Catalyst Supported on γ-Alumina: Influence of Pt-Pd Ratio on the Catalytic Activity. *Appl. Catal., A* **2005**, 280 (2), 125–131.
- (16) Tang, W.; Deng, Y.; Li, W.; Li, J.; Liu, G.; Li, S.; Wu, X.; Chen, Y. Importance of Porous Structure and Synergistic Effect on the Catalytic Oxidation Activities over Hierarchical Mn-Ni Composite Oxides. *Catal. Sci. Technol.* **2016**, *6* (6), 1710–1718.
- (17) Bai, G.; Dai, H.; Deng, J.; Liu, Y.; Ji, K. Porous NiO Nanoflowers and Nanourchins: Highly Active Catalysts for Toluene Combustion. *Catal. Commun.* **2012**, *27*, 148–153.
- (18) Li, W. B.; Wang, X. J.; Gong, X. Catalytic Combustion of VOCs on Non-Noble Metal Catalysts. *Catal. Today* **2009**, *148*, 81–87.
- (19) Li, L.; Liu, S.; Liu, J. Surface Modification of Coconut Shell Based Activated Carbon for the Improvement of Hydrophobic VOC Removal. *J. Hazard. Mater.* **2011**, *192* (2), 683–690.
- (20) Park, E. J.; Lee, J. H.; Kim, K. D.; Kim, D. H.; Jeong, M. G.; Kim, Y. D. Toluene Oxidation Catalyzed by NiO/SiO<sub>2</sub> and NiO/TiO<sub>2</sub>/SiO<sub>2</sub>: Towards Development of Humidity-Resistant Catalysts. *Catal. Today* **2016**, *260*, 100–106.
- (21) Lee, H. J.; Seo, H. O.; Kim, D. W.; Kim, K. D.; Luo, Y.; Lim, D. C.; Ju, H.; Kim, J. W.; Lee, J.; Kim, Y. D. A High-Performing Nanostructured  ${\rm TiO_2}$  Filter for Volatile Organic Compounds Using Atomic Layer Deposition. *Chem. Commun.* **2011**, 47 (19), 5605–5607.
- (22) Soonmin, H.; Vanalakar, S. A.; Galal, A.; Singh, V. N. A Review of Nanostructured Thin Films for Gas Sensing and Corrosion Protection. *Mediterr. J. Chem.* **2018**, *7* (6), 433–451.
- (23) Adebayo, B. O.; Lawson, S.; Rownaghi, A. A.; Rezaei, F. Analysis of Equilibrium and Dynamic Adsorption of Benzene Vapor over Unimodal and Bimodal Silica-Based Mixed-Metal Oxides. *Chem. Eng. J.* **2020**, 396, 125273.
- (24) Liang, X.; Hakim, L. F.; Zhan, G. D.; McCormick, J. A.; George, S. M.; Weimer, A. W.; Spencer, J. A.; Buechler, K. J.; Blackson, J.; Wood, C. J.; Dorgan, J. C. Novel Processing to Produce Polymer/Ceramic Nanocomposites by Atomic Layer Deposition. *J. Am. Ceram. Soc.* **2007**, *90* (1), 57–63.

- (25) D'Amico, A. D.; Wu, D.; Hodgin, H. J. Vapor Purification for the Micromeritics 3FLEX, 2015, pp 1-4
- (26) Soto-Cantu, E.; Cueto, R.; Koch, J.; Russo, P. S. Synthesis and Rapid Characterization of Amine-Functionalized Silica. *Langmuir* **2012**. 28, 5562–5569.
- (27) Munasir; Triwikantoro; Zainuri, M.; Darminto. Synthesis of SiO<sub>2</sub> Nanopowders Containing Quartz and Cristobalite Phases from Silica Sands. *Mater. Sci.-Pol.* **2015**, 33, 47.
- (28) Miguel, C. V.; Trujillano, R.; Rives, V.; Vicente, M. A.; Ferreira, A. F. P.; Rodrigues, A. E.; Mendes, A.; Madeira, L. M. High Temperature CO<sub>2</sub> Sorption with Gallium-Substituted and Promoted Hydrotalcites. *Sep. Purif. Technol.* **2014**, *127*, 202–211.
- (29) Haskouri, J. El; Dallali, L.; Fernández, L.; Garro, N.; Jaziri, S.; Latorre, J.; Guillem, C.; Beltrán, A.; Beltrán, D.; Amorós, P. ZnO Nanoparticles Embedded in UVM-7-like Mesoporous Silica Materials: Synthesis and Characterization. *Phys. E* **2009**, 42 (1), 25–31.
- (30) Sing, K. S. W. Reporting Physisorption Data for Gas/Solid Systems with Special Reference to the Determination of Surface Area and Porosity (Provisional). *Pure Appl. Chem.* **1982**, *54* (11), 2201–2218.
- (31) Ortiz De Zárate, D.; Gómez-Moratalla, A.; Guillem, C.; Beltrán, A.; Latorre, J.; Beltrán, D.; Amorós, P. High-Zirconium-Content Nano-Sized Bimodal Mesoporous Silicas. *Eur. J. Inorg. Chem.* **2006**, 2006, 2572–2581.
- (32) Babaie, F.; Mousavi, S. H.; Alizadeh, A. M.; Hazrati, N. Carbon Dioxide Capture by Modified UVM-7 Adsorbent. *J. Chem. Pet. Eng.* **2014**, *48* (2), 91–102.
- (33) Smått, J. H.; Schunk, S.; Lindén, M. Versatile Double-Templating Synthesis Route to Silica Monoliths Exhibiting a Multimodal Hierarchical Porosity. *Chem. Mater.* **2003**, *15* (12), 2354–2361.
- (34) Goma, D.; Delgado, J. J.; Lefferts, L.; Faria, J.; Calvino, J. J.; Cauqui, M. Á. Catalytic Performance of Ni/CeO<sub>2</sub>/X-ZrO<sub>2</sub> (X = ca, y) Catalysts in the Aqueous-Phase Reforming of Methanol. *Nanomaterials* **2019**, 9 (11), 1582.
- (35) Seo, H. O.; Kim, D. H.; Kim, K. D.; Park, E. J.; Sim, C. W.; Kim, Y. D. Adsorption and Desorption of Toluene on Nanoporous TiO<sub>2</sub>/SiO<sub>2</sub> Prepared by Atomic Layer Deposition (ALD): Influence of TiO<sub>2</sub> Thin Film Thickness and Humidity. *Adsorption* **2013**, *19* (6), 1181–1187.
- (36) Hengne, A. M.; Samal, A. K.; Enakonda, L. R.; Harb, M.; Gevers, L. E.; Anjum, D. H.; Hedhili, M. N.; Saih, Y.; Huang, K. W.; Basset, J. M. Ni-Sn-Supported ZrO<sub>2</sub> Catalysts Modified by Indium for Selective CO<sub>2</sub> Hydrogenation to Methanol. *ACS Omega* **2018**, 3 (4), 3688–3701.
- (37) Biesinger, M. C.; Payne, B. P.; Lau, L. W. M.; Gerson, A.; Smart, R. S. C. X-Ray Photoelectron Spectroscopic Chemical State Quantification of Mixed Nickel Metal, Oxide and Hydroxide Systems. *Surf. Interface Anal.* **2009**, 41 (4), 324–332.
- (38) Tyagi, B.; Kalpesh; Sidhpuria, B.; Basha; Raksh, S.; Jasra, V. Effect of Zr/Si Molar Ratio and Sulfation on Structural and Catalytic Properties of ZrO<sub>2</sub>-SiO<sub>2</sub> Mixed Oxides. Springer: Berlin.
- (39) Al-Mamoori, A.; Rownaghi, A. A.; Rezaei, F. Combined Capture and Utilization of CO<sub>2</sub> for Syngas Production over Dual-Function Materials. *ACS Sustainable Chem. Eng.* **2018**, 6 (10), 13551–13561.
- (40) Ncube, T.; Kumar Reddy, K. S.; Al Shoaibi, A.; Srinivasakannan, C. Benzene, Toluene, m-Xylene Adsorption on Silica-Based Adsorbents. *Energy Fuels* **2017**, *31* (2), 1882–1888.
- (41) Seo, H. O.; Sim, C. W.; Kim, K.-D.; Kim, Y. D.; Lim, D. C. Nanoporous TiO<sub>2</sub>/SiO<sub>2</sub> Prepared by Atomic Layer Deposition as Adsorbents of Methylene Blue in Aqueous Solutions. *Chem. Eng. J.* **2012**, *183*, 381–386.
- (42) Szulejko, J. E.; Kim, K. H.; Parise, J. Seeking the Most Powerful and Practical Real-World Sorbents for Gaseous Benzene as a Representative Volatile Organic Compound Based on Performance Metrics. Sep. Purif. Technol. 2019, 212, 980–985.
- (43) Kim, K. H.; Szulejko, J. E.; Raza, N.; Kumar, V.; Vikrant, K.; Tsang, D. C. W.; Bolan, N. S.; Ok, Y. S.; Khan, A. Identifying the Best

Materials for the Removal of Airborne Toluene Based on Performance Metrics - A Critical Review. *Journal of Cleaner Production*. Elsevier Ltd.: Amsterdam, 2019.

- (44) Adebayo, B. O.; Krishnamurthy, A.; Rownaghi, A. A.; Rezaei, F. Toluene Abatement by Simultaneous Adsorption and Oxidation over Mixed-Metal Oxides. *Ind. Eng. Chem. Res.* **2020**, *59*, 13762.
- (45) Mokhatab, S.; Poe, W.; Mak, J. Handbook of Natural Gas Transmission and Processing; Elsevier: Amsterdam, 2006; p xxi.
- (46) Rostami, R.; Jonidi Jafari, A. Application of an Adsorptive-Thermocatalytic Process for BTX Removal from Polluted Air Flow. *J. Environ. Health Sci. Eng.* **2014**, *12*, 89.